

# Performance of the MICE diagnostic systems

5

A.N. Other et al.

This paper will describe:

- The detectors as we have it installed in the MICE Hall at November 2017
- The performances of the detectors
- The absorbers models and their validation
- The track matching

10

We'll make reference to the published papers wherever possible.

We're targeting the JINST volume.

## 1 Introduction

To include:

15

- Motivation
- Outline of the experiment

## 2 Time-of-Flight Detectors

List of figures

20

- PMT charge correlation PMT0 vs PMT1 - maybe, if relevant
- TW calibration of one channel
- Slab DT before TW correction and after - single pixel.
- Residual TW
- T0 correction for 1 channel - electron peak fit
- Slab DT mean and sigma for all pixels after calibration
- Overall slab DT
- Space-point creation efficiency per pixel/slab
- Particle detection efficiency - don't know how to extract from the data, ideally pixel map for each TOF

25

### 2.1 Introduction

30

Three time-of-flight detectors (TOF0, TOF1, TOF2) have been built and installed at RAL in 2008 and 2009 to measure the position and the time of crossing particles. TOF0 and TOF1 [1], [2], [3] are placed upstream of the cooling channel, and TOF2 [4] is downstream of the channel, mounted in front of the KL, as shown in Fig. ???. The time of flight between two TOF stations provides particle identification information and can also be used for momentum measurement. TOF1 served most of the time also as an experimental trigger. They have smoothly operated during the so-called Step I and Step IV [5], [6] running periods of the MICE experiment and were essential for all the measurements done.

35

The good performances of the TOF detectors, over an extended period of time, has enabled the MICE experiment to characterize fully its muon beams during Step I data-taking, by measuring their emittance [7] and assessing their pion contamination [8].

Each TOF station is made of two planes of fast 1" thick scintillator counters along X/Y directions (to increase measurement redundancy) read out at both edges by R4998 Hamamatsu fast photomultiplier tubes<sup>1</sup>. R4998 PMTs have been delivered by Hamamatsu in assemblies (H6533MOD) that include the PMT tube, the voltage divider chain and a 1 mm thick  $\mu$ -metal shield, extending 30 mm beyond the photocathode surface. TheTo increase the count rate stability active dividers were used, instead of conventional resistive ones. A simple design with flat fish-tail PMMA light guides, as respectopposed to tilted ones (to reduce the influence of magnetic field) or Winston cones, has been chosen to optimize the timing detector resolution (favouring the collection of straight light) and to allow an easy mechanical assembly. *any picture or reference here?* TOF0, TOF1, and TOF2 have active areas of  $40 \times 40 \text{ cm}^2$ ,  $42 \times 42 \text{ cm}^2$ , and  $60 \times 60 \text{ cm}^2$  respectively. The slabs in TOF0 are 4 cm wide, while the slabs of TOF1 and TOF2 are 6 cm wide respectively. The PMTs signal, after  $\sim 34$  m long RG213 cable and a 50% – 50% passive splitter, arrive to a leading-edge CAMAC Lecroy 4115 discriminator followed by a CAEN V1290 TDC for time measurements and to a CAEN V1724 FADC for pulse-height measurements, to correct time-walk. As reported in reference [2], RG213 cables<sup>2</sup> have a better temperature stability than conventional RG58 cables. Their delay have been individually measured in laboratory, before installation in the experimental hall. Time calibration of individual counters has been done with impinging beam particles by using the detector X/Y redundancy [9]. *This is too vague. Calibration will be covered later. What does counter refer to here?*

Due to the low residual magnetic field produced by the last quadrupole of the beam line in the proximity of the TOF0 detector ( $\leq 50$  G), the used conventional PMTs had to use elongated  $\mu$ -metal shielding. The other two TOF stations (TOF1/TOF2) had to work instead in the stray fields of the cooling channel solenoids, that are only partially shielded by a 100 mm thick annular iron plates. As residual magnetic fields are up to 0.13 T (with a component along the PMTs axis up to 0.04 T), a local or global magnetic shielding for TOF1 and TOF2 detectors had to be envisaged. The local shielding option was chosen, at the end, for convenience and easiness of implementation. As magnetic shielding is a mass effect, box-shaped soft iron shielding are more effective than cylindrical ones. This idea pioneered in the D0 experiment has been tested in the case of MICE using different geometrical configuration for the iron shielding boxes and different iron materials (e.g. Fe360, ARMCO<sup>3</sup>, etc). The problem is usually the longitudinal component of the magnetic field, while the orthogonal component may be more easily shielded. Systematic studies have been done, using a built on purpose solenoid of 23 cm inner diameter, 40 cm length<sup>4</sup> and are fully reported in reference [10]. A composite structure based on the 1 mm  $\mu$ -metal shielding of the H6533Mod assemblies and an external additional  $6 \times 6 \text{ cm}^2$  ( $5.6 \times 5.6 \text{ cm}^2$ ) ARMCO box, 15 cm long, with an internal hole of 3.2 cm diameter has been adopted for the PMT's magnetic shielding of TOF2 (TOF1) [11]. Fig. 1 show how the local shielding has been implemented in TOF2, using different sheets of ARMCO to make a “single bar structure” for all the PMTs of one side, instead of single boxes for individual PMTs. The effective shielding amounts to  $\sim 6.6$  cm of ARMCO thickness, with extra shielding effect due to the fact that all bars shielding the TOF2 PMTs are magnetically linked between them and to both the KL shielding and the shielding plate making a single magnetic loop. Fig. 2 shows some steps of the assembly procedure for the TOF2 detector at INFN MIB mechanics workshop.

*The paragraph above is rather detailed, with many things that could be explained incorrectly. Should be made brief, unless full technical design description is required.*

*The following paragraph is summarising the performance. It states overly optimistic performance.*

For what attains performances, TOF0, TOF1, and TOF2 had timing resolutions around 50-60 ps respectively (*currently observed  $\sim 110$  ps*), over the 8 years running period, consistent with design requirements, with the

<sup>1</sup>one-inch linear focused PMTs with 10 stages, typical gain  $G \sim 5.7 \times 10^6$  at -2250 V and B=0 T, rise time 0.7 ns, transit time spread (TTS)  $\sim 160$  ps

<sup>2</sup>CERN type C-50-6-1, with rated delay 4.08 ns/m

<sup>3</sup>ARMCO steel from AkSteel is a pure iron with a maximal carbon content of 0.025% and very high magnetic saturation

<sup>4</sup>built by TBM srl, Uboldo (VA), Italy

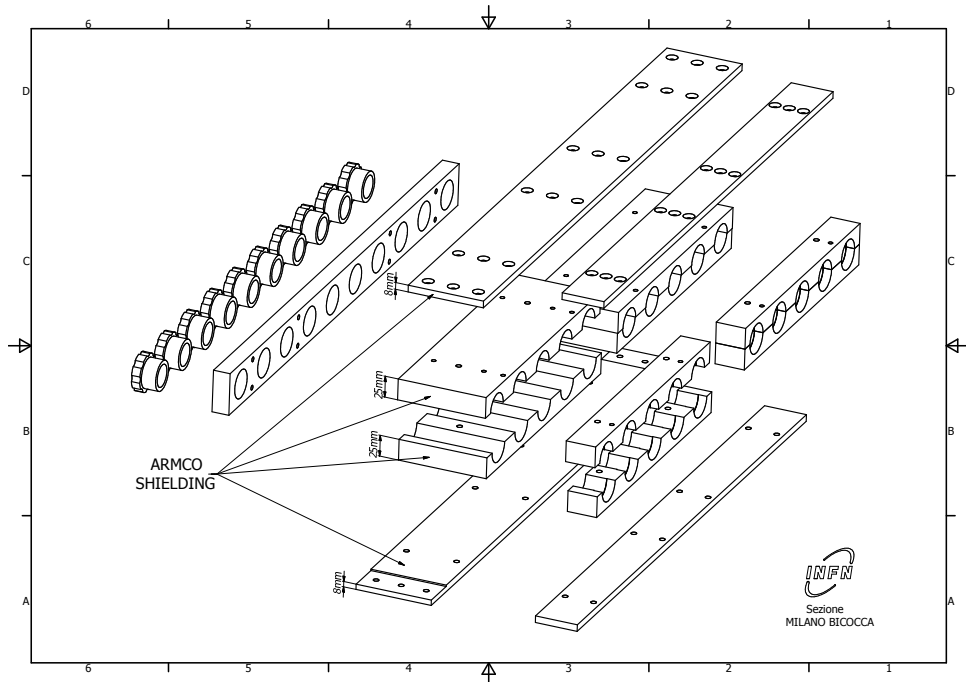


Figure 1: Exploded view of the TOF2 detector magnetic shielding for one row of PMTs.



Figure 2: Assembly of TOF2 at INFN MIB mechanics workshop. Left to right: from the bare magnetic shielding to the installed counters of a plane.

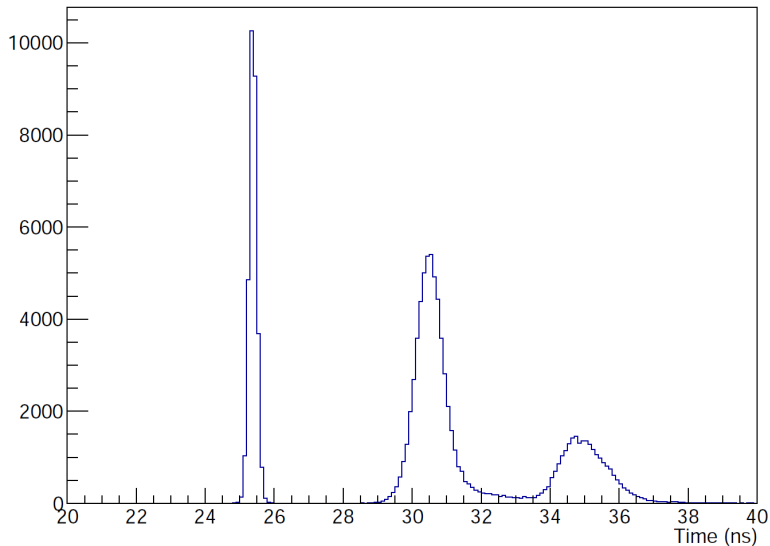


Figure 3: Time of flight between TOF0 and TOF1 for a “pion” beam. From the left: the well separated electron, muon and pion peaks.

spatial resolution around 1 cm. *We don't use any special reconstruction method. Resolution kept at 4 cm or 6 cm for TOF0 or TOF1 and TOF2 respectively. Do we say resolution = 1/2 of strip width or  $1/\sqrt{12}$ ?* Fig. 3 shows distributions of the time of flight between TOF0 and TOF1 where electrons, muons and pions fall into three well defined peaks.

<sup>85</sup> *What is currently the main purpose of TOFs? This determines the requirements on the performance. Will need to tell that current T-o-F measurement has sufficient resolution, which appears to be  $\sim$ 100-120 ps*

## 2.2 TEMPORARY - Plots

### 2.3 Calibration Method

Describe the method. Based on MICE note 251.

<sup>90</sup> *TOF NIMA paper says that measured time resolution of the CAEN TDC was 22 ps/count, as opposed to declared 25 ps!*

Some description of the calibration method is also described in the paper.

#### 2.3.1 Time Walk Correction

<sup>95</sup> *Fig of a selected PMT TW 2D hist. + Profile + Fit Fig of residual TW. Fig of Slab DT before TW correction and after.*

Time walk was considered to be constant property of each channel. The same correction was used for all runs.

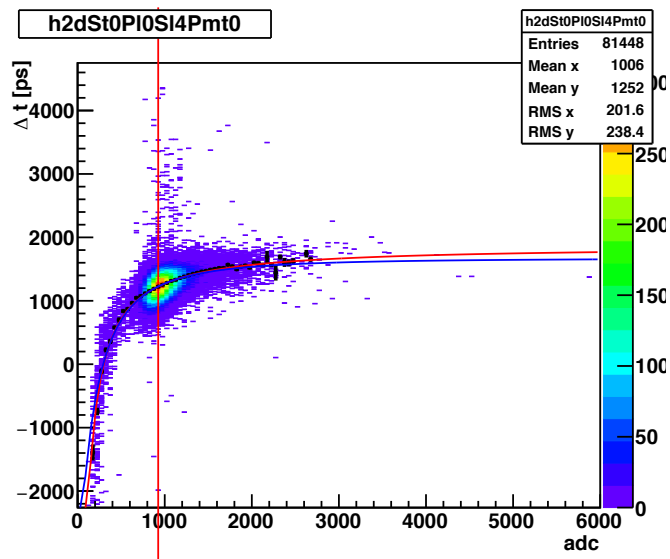


Figure 4:

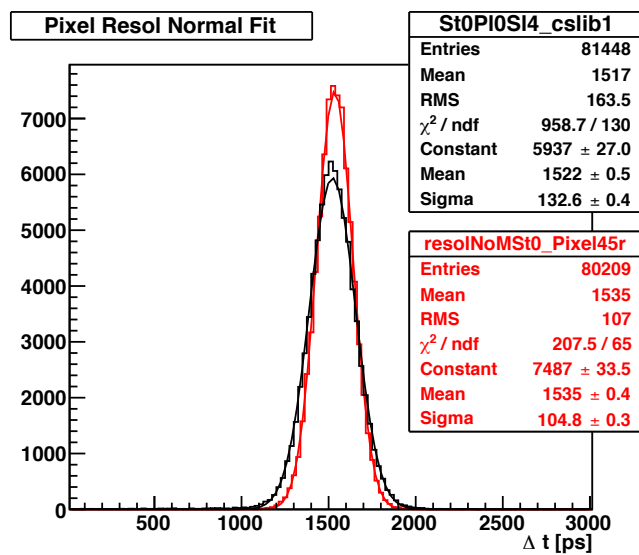


Figure 5:

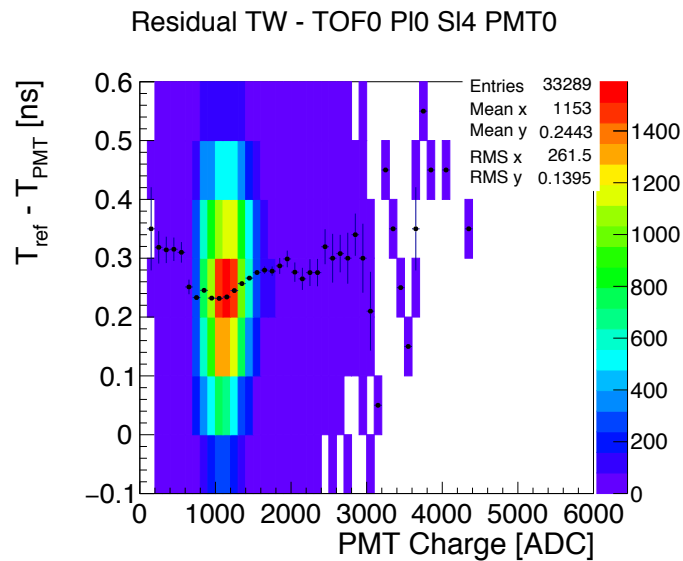


Figure 6:

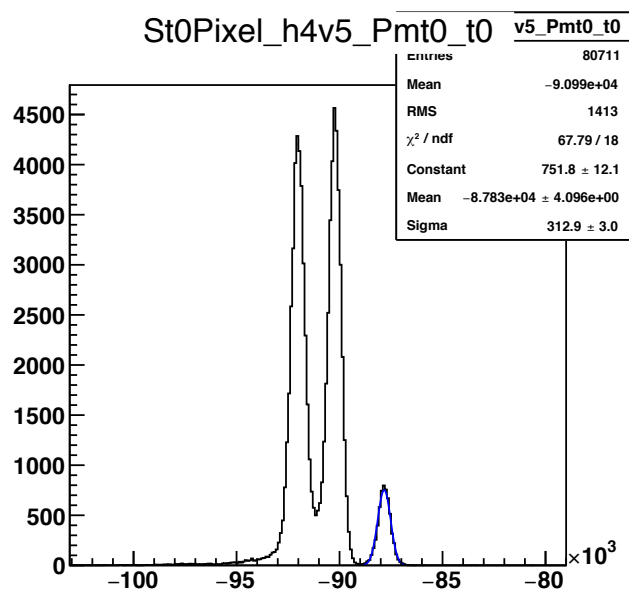


Figure 7:

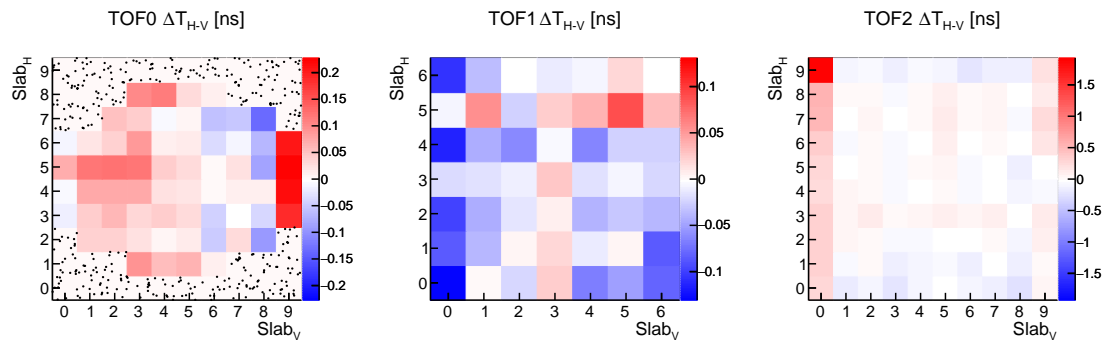


Figure 8:

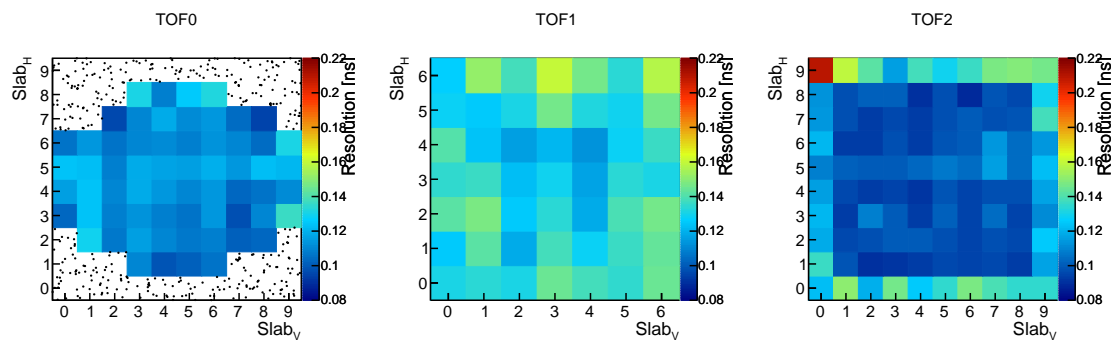


Figure 9:

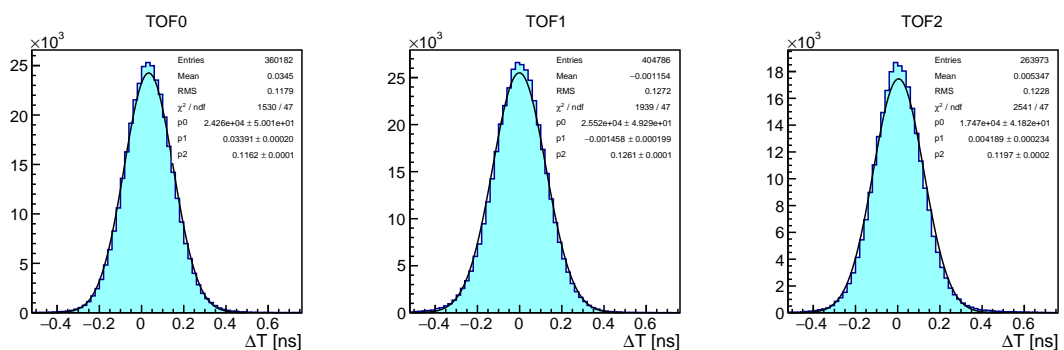


Figure 10:

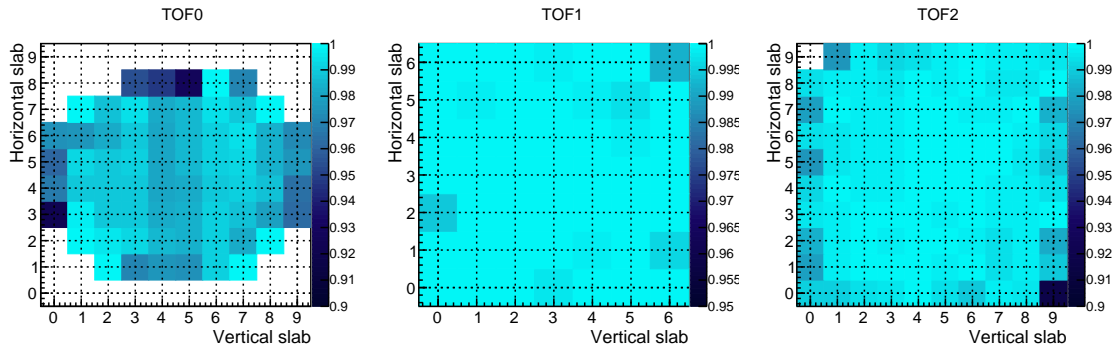


Figure 11:

### 2.3.2 Trigger Delay Correction

### 2.3.3 T0 Correction

## 100 2.4 Reconstruction

### 2.5 Performance

*Several figures are already in the TOF NIMA paper.*

Figures to show up here:

- Slab DT - selected slabs/counters + overall TOFs
- 105 • ToF10 - + detail of electron peak
- Space-point reconstruction efficiency - shows that slab hits are within the required cut, inefficiency from only single slabs hit by different particles in the given spill/bunch
- particle detection efficiency - how to show?

### 2.5.1 Low-level Characterisation

- 110 • PMT charge correlation PMT0 vs PMT1 - maybe, if relevant
- Residual TW - this should go to the calibration section
- Slab DT

### 2.5.2 Time-of-Flight Resolution and Efficiency

- Resolution
  - Slab DT for all TOFs, show similar performance, although they have different construction.
- 115 • Efficiency

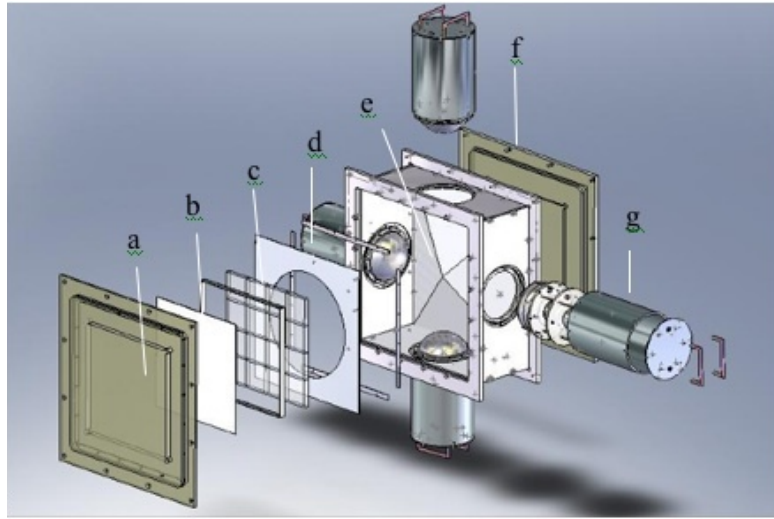


Figure 12: MICE aerogel Cherenkov counter blowup: a) entrance window, b) mirror, c) aerogel mosaic, d) acetate window, e) GORE reflector panel, f) exit window and g) 8 inch PMT in iron shield.

### 3 Cherenkov Detectors

#### 3.1 Introduction

The Cherenkov detectors are primarily designed to provide  $\pi$ - $\mu$  separation in the higher momentum ranges,  
120 where TOF separation is not sufficient for conclusive particle identification.

In order to provide separation over a large range of momenta, two high density silica aerogel Cherenkov  
detectors (CkovA and CkovB) with refractive indices  $n=1.07$  and  $n=1.12$  are used. They are each read out by  
four 200 mm photomultiplier tubes and placed directly one after another in the beamline, located just after the  
first TOF counter. In Fig. 12 an exploded view of one detector is shown.

125 Their respective thresholds provide different responses in four distinct momentum ranges, i.e. in the 200  
MeV/c beams, pions are below the threshold which would fire the detector for both CkovA and CkovB whereas  
muons are above only for CkovB, while for the 240 MeV/c beams, pions are above the threshold for CkovB  
while muons are above for both CkovA and CkovB. Using this information algorithms can be written that  
produce likelihood distributions of particle type. Below the CkovB muon threshold of about 217.9 MeV/c,  
130 where there is no separation, the TOFs provide good separation, whereas the momentum range above the  
CkovA pion threshold (367.9) MeV/c is outside of the MICE running parameters [12].

#### 3.2 Performance

### 4 KLOE-Light Calorimeter

#### 4.1 Introduction

135 The KLOE-Light (KL) pre-shower sampling calorimeter is composed of extruded lead foils in which scintillating  
fibres are placed in volume ratio scintillator:lead  $\sim 2:1$ , “lighter” than the one of the KLOE experiment  
calorimeter (1:1).

The fibres are 1 mm diameter BICRON BCF-12, scintillating in the blue, 1.35 mm distant from each other

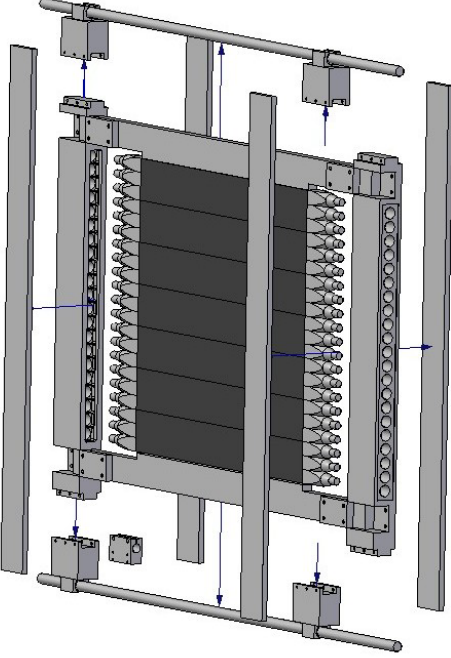


Figure 13: Magnetic shielding of KLOE-Light PMTs.

within a layer. The distance between two layers is 0.98 mm, one layer being shifted by half the fibre pitch with respect to the next. Scintillation light is guided from each slab into a total of six PMTs (three on each side). Iron shields are fitted to each photomultiplier to mitigate against large stray magnetic fields from the cooling channel (see Fig. 13). The signal from each PMT is sent to a shaping amplifier (SA) module, which shapes and stretches the signal in time in order to match the sampling rate of the flash ADCs (Fig. 14 shows the design of a single slab). A total of 7 slabs forms the whole detector, which has an active volume of  $93\text{ cm} \times 93\text{ cm} \times 4\text{ cm}$ .

With its 2.5 radiation lengths the KL is used to distinguish muons from decay electrons providing energy deposition and timing information and to act as pre-shower in front of the EMR. The detector has been used to estimate the level of pion contamination within the MICE muon beams to be around 1% [8].

## 4.2 Performance

The study of KL response to different particle types at different momenta is based on particle identification obtained by time-of-flight detector, as shown in the example of Fig. 3, by applying proper cuts on the time-of-flight spectrum. The performance is presented for 140, 170, 200, 240 and 300 MeV/c momenta at the absorber position, and depending of species population for muons, pions and electrons. The results presented below are obtained from the straight tracks data (i.e. without magnetic fields in the trackers or focus coil) taken mainly in 2017. The KL response to muons, pions and electrons for all available momenta is presented in Fig. 15. It is clear in the cases of muons and pions that they are below mip momenta since energy deposition decreases with momentum increasing<sup>5</sup>.

---

<sup>5</sup>Actually the energy deposition is defined as the sum of ADC products from all cells in KL above a given threshold. The ADC product on the other hand is the product of left and right side of one slab divided by the sum of left and right side:  $ADC_{prod} = 2 \times ADC_{left} \times ADC_{right} / (ADC_{left} + ADC_{right})$ . The factor 2 is present for normalization. The product of two sides compensates the effect of attenuation.

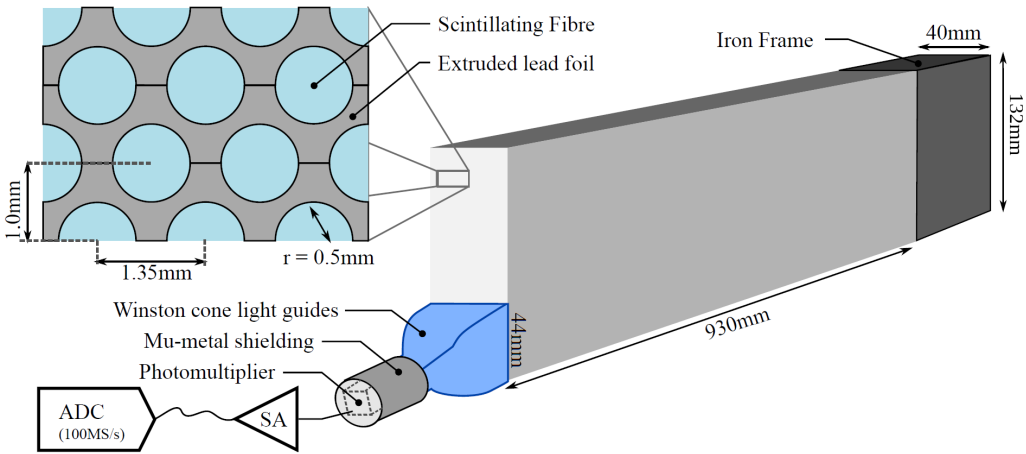


Figure 14: Single slab design of MICE KLOE-Light Calorimeter.

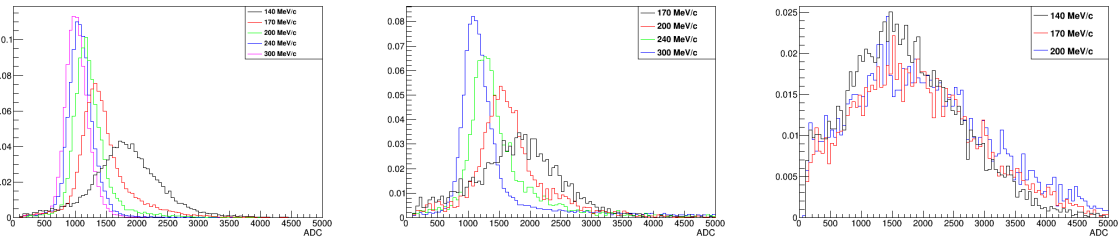


Figure 15: KL response to muons (left), pions (centre) and electrons (right) for several momenta. It is shown charge deposited by particles in KL in arbitrary units. All histograms are normalized to unity.

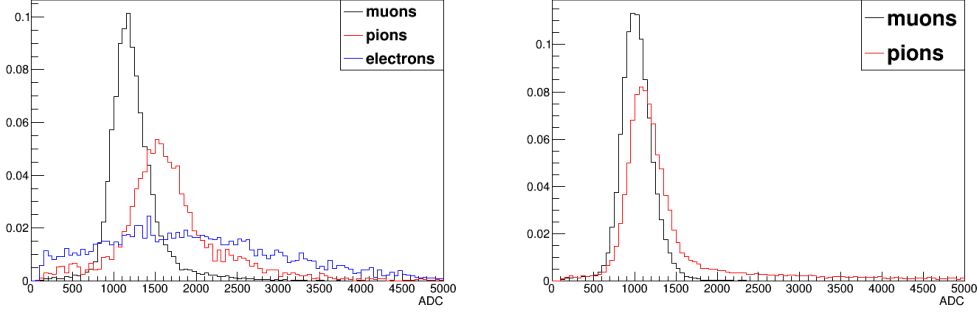


Figure 16: Comparison of energy deposition of muons, pions and electrons at 200 MeV/c (left) and of muons to pions at 300 MeV/c (right).

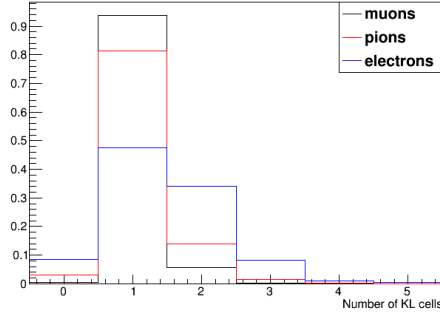


Figure 17: Particle multiplicity for 240 MeV/c, i.e. number of KL cells fired.

For comparison of energy deposition of muon, pions and electrons for fixed momentum Fig. 16 is presented. In the case of 300 MeV/c (Fig. 16, right), where muons and pions have almost the same maximum of distribution, the tail of pions is fatter than muon one. This is due to the fact that pions experience strong interaction as well. This pion behaviour has been used to estimate its contamination in muon sample.

The number of fired KL cells by a single muon, electron or pion is given in Fig. 17 for 240 MeV/c beam. For muons we expect one, in some cases two and almost never more fired cells depending on track inclination. Pions and electrons create avalanches in KL and electron ones is much wider than the pion ones as visible of number of KL cell hits. The same figure shows number of events when if there is a reconstructed TOF track, but no signal in KL above the threshold. This can be used to calculate efficiency of KL for the three species as a function of momentum. The results are presented in Table 1 and shows that efficiency for muon registration is close to 99%.

| <b>species</b>   | <b>140 MeV/c</b> | <b>170 MeV/c</b> | <b>200 MeV/c</b> | <b>240 MeV/c</b> | <b>300 MeV/c</b> |
|------------------|------------------|------------------|------------------|------------------|------------------|
| <b>electrons</b> | $0.95 \pm 0.02$  | $0.95 \pm 0.01$  | $0.94 \pm 0.03$  | n/a              | n/a              |
| <b>muons</b>     | $0.97 \pm 0.02$  | $0.99 \pm 0.01$  | $0.99 \pm 0.01$  | $0.99 \pm 0.01$  | $0.99 \pm 0.01$  |
| <b>pions</b>     | n/a              | $0.89 \pm 0.03$  | $0.95 \pm 0.03$  | $0.97 \pm 0.03$  | $0.98 \pm 0.01$  |

Table 1: Efficiency of KL for electrons, muons and pions as a function of particle momentum. The conditions required are existing of a TOF track and signal in KL above the threshold. The uncertainties are statistical.

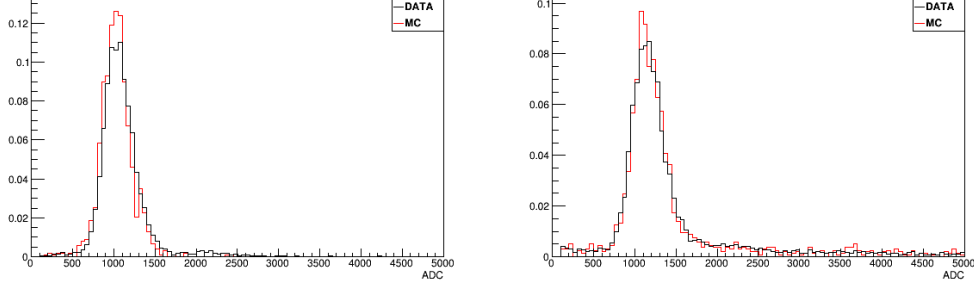


Figure 18: Comparison between data and Monte Carlo simulation of KL response to muons (left) and pions (right) at 300 MeV/c.

In Fig. 18 is shown simulation of KL response to 300 MeV/c muons and pions and the distributions are compared with data. The agreement between data and simulation is very good. The simulation is done via following steps:

- Smearing of produced photons in scintillator fibres. They obtain Poisson statistic so such is applied. In principle one can replace it with Gaussian because the number of photons created is large enough for such an approximation.
- Photoelectrons created on photomultiplier photocathode also have Poisson statistics. It cannot be replaced here with normal distribution because the number of photoelectrons is small enough so such an approximation is illegal.
- Photomultiplier gain obtains also statistical properties but it is neither Poisson nor gauss. Nevertheless it turns out that for simplicity one can use Gaussian distribution with mean value equals to PMT gain and sigma of distribution equals to half of the gain. KL photomultipliers have gain  $\sim 2 \times 10^6$ , so their sigma is simply  $10^6$ .

## 5 Electron Muon Ranger

### 5.1 Introduction

The Electron-Muon Ranger (EMR) is a fully-active scintillator detector [13]. It can be classified as a tracking-calorimeter as its granularity allows for track reconstruction. The EMR consists of extruded triangular scintillator bars arranged in planes. One plane contains 59 bars and covers an area of  $1.27 \text{ m}^2$ . Each even bar is rotated by 180 degrees with respect to the odd one. A cross-section of bars and their arrangement in a plane is shown in Fig. 19. This configuration does not leave dead area in the detector for particles crossing a plane with angles that do not exceed 45 degrees with respect to the beam axis. Each plane is rotated through 90 degrees with respect to the previous one, such that a pair of planes defines a horizontal and vertical ( $x, y$ ) interaction coordinate. The light, produced when a particle crosses a bar, is collected by a wave-length shifting (WLS) fibre glued inside the bar. At both ends, the WLS fibre is coupled to clear fibres that transport the light to a photomultiplier tube (PMT). Signals produced in a plane are read out collectively on one end by a single-anode PMT for an integrated charge measurement and separately on the other by a multi-anode PMTs for individual bar hit reconstruction. The full detector is composed of 24 X-Y modules for a total active volume of  $\sim 1 \text{ m}^3$ .

An array of analyses were conducted to characterize the hardware of the EMR and determine whether the detector performs to specifications [14]. The clear fibres coming from the bars were shown to transmit the

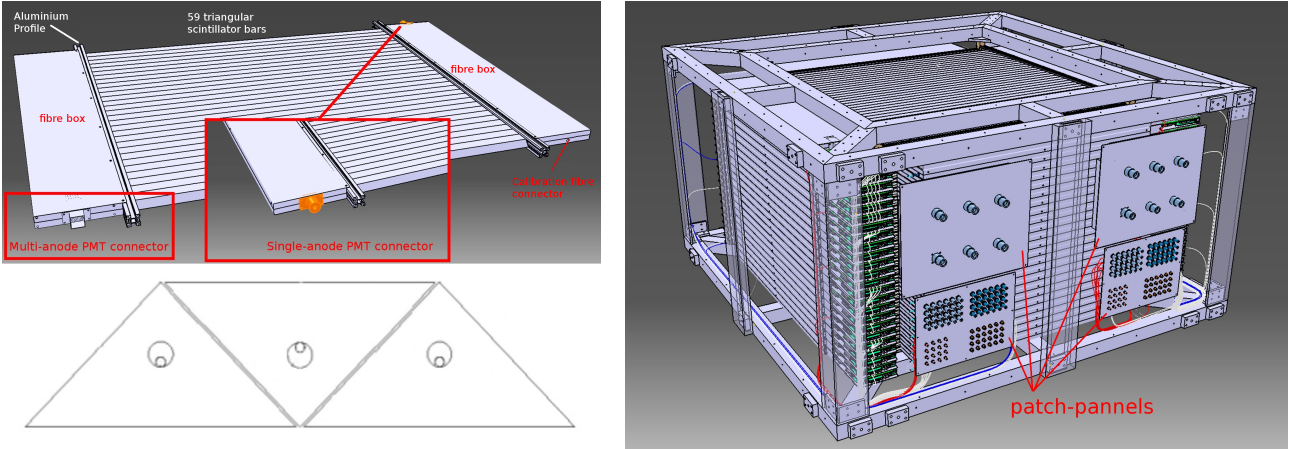


Figure 19: Drawing of one EMR plane (top left), cross section of 3 bars and their wavelength shifting fibres (bottom left) and drawing of the full detector (right).

desired amount of light, and only four dead channels were identified in the electronics. Two channels had indubitably been mismatched during assembly and the DAQ channel map was subsequently corrected. The level of crosstalk is within acceptable values for the type of multi-anode photomultiplier used with an average of  $0.20 \pm 0.03\%$  probability of occurrence in adjacent channels and a mean amplitude equivalent to  $4.5 \pm 0.1\%$  of the primary signal intensity. The efficiency of the signal acquisition, defined as the probability of recording a signal in a plane when a particle goes through it in beam conditions, reached  $99.73 \pm 0.02\%$ .

The primary purpose of the EMR is to distinguish between muons and their decay products, identifying muons that have crossed the entire cooling channel. Muons and electrons exhibit distinct behaviours in the detector. A muon follows a single straight track before either stopping or exiting the scintillating volume, while electrons shower in the lead of the KL and create a broad cascade of secondary particles. Two main geometric variables, the plane density and the shower spread, are used to differentiate them. The detector is capable of identifying electrons with an efficiency of 98.6 %, providing a purity for the MICE beam that exceeds 99.8 %. The EMR also proved to be a powerful tool for the reconstruction of muon momenta in the range 100–280 MeV/c [15].

## 5.2 Performance

## 6 The Trackers

### 6.1 The Hardware

MICE is equipped with two identical, high precision scintillating-fibre ("sciFi") trackers, described in [1]. Each tracker is placed in a superconducting solenoid designed to provide a uniform field over the tracking volume. One tracker, TKU, is upstream of the cooling cell, the other, TKD, downstream. Each tracker consists of five detector stations, labelled 1 to 5, with the stations placed varying distances apart to help resolve ambiguities. The trackers are placed symmetrically about the cooling cell, with station 1 the nearest to the cooling cell for both. Each station is formed of three planes of  $350\mu m$  scintillating-fibres, orientated at 120 degrees to one another. Each plane consists of two layers. The fibres in each plane butt up to each other and the two layers are offset with respect to each other by a fibre radius. A charge particle will then deposit energy in at least  $350\mu m$  of scintillator, providing uniform response over the whole station face. The doublet layers are glued

to a sheet of mylar and the fibres are adjacent groups of seven fibres form one read-out channel. The three views are referred to as U, V and W, with the order being identical for each station and the U fibres running vertically. The light from the seven scintillating fibres passes into a single clear fibre, which takes it to a visible light photon counter (VLPC) which operate at 9k. The signal from the VLPCs is digitised using electronics developed by the D0 collaboration[2].

## 6.2 Tracker Performance and Reconstruction

### 6.2.1 Low Level Analysis

Low level analysis including digits, to spacepoints, 2 pages, Melissa U.

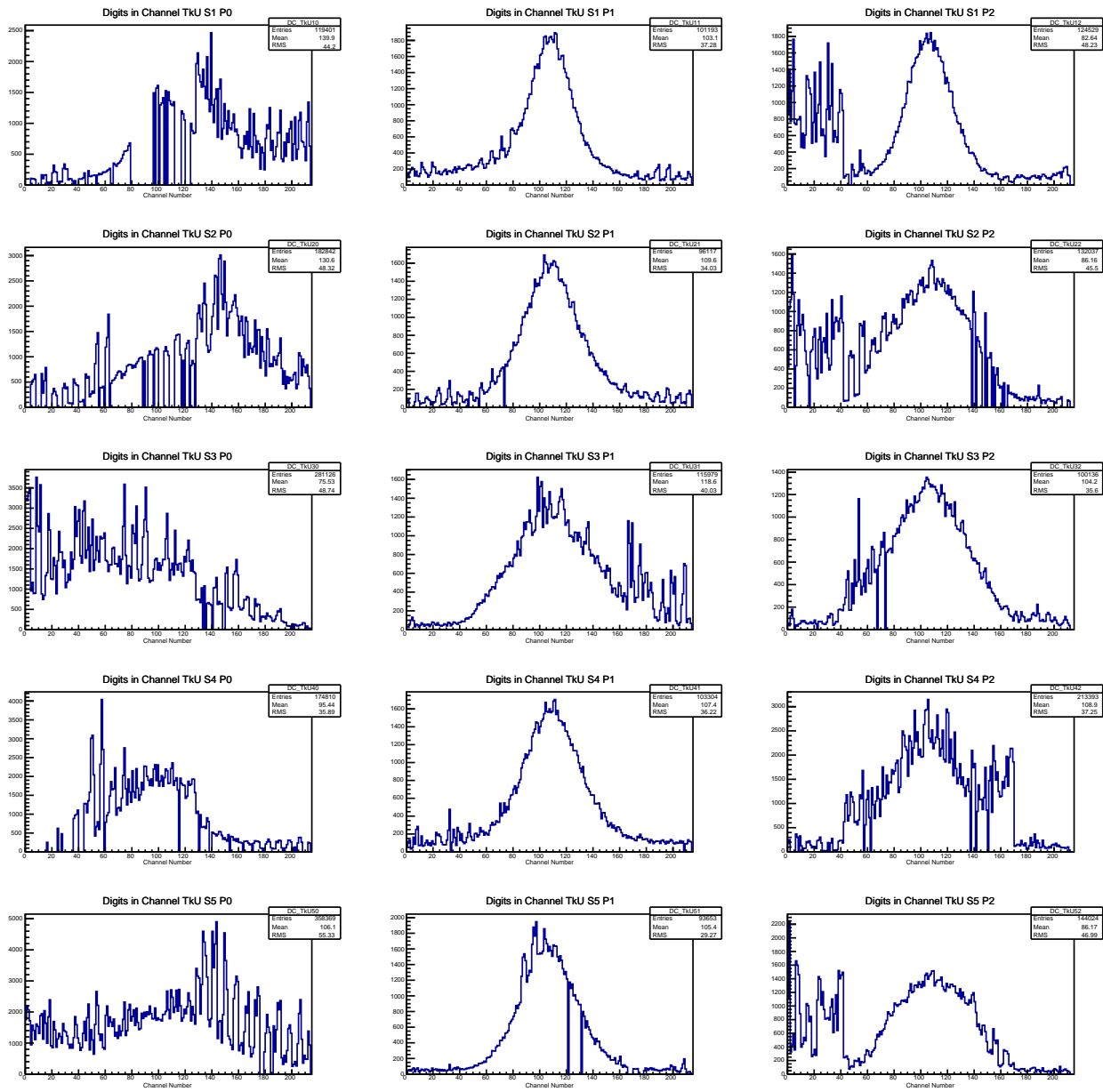


Figure 20:

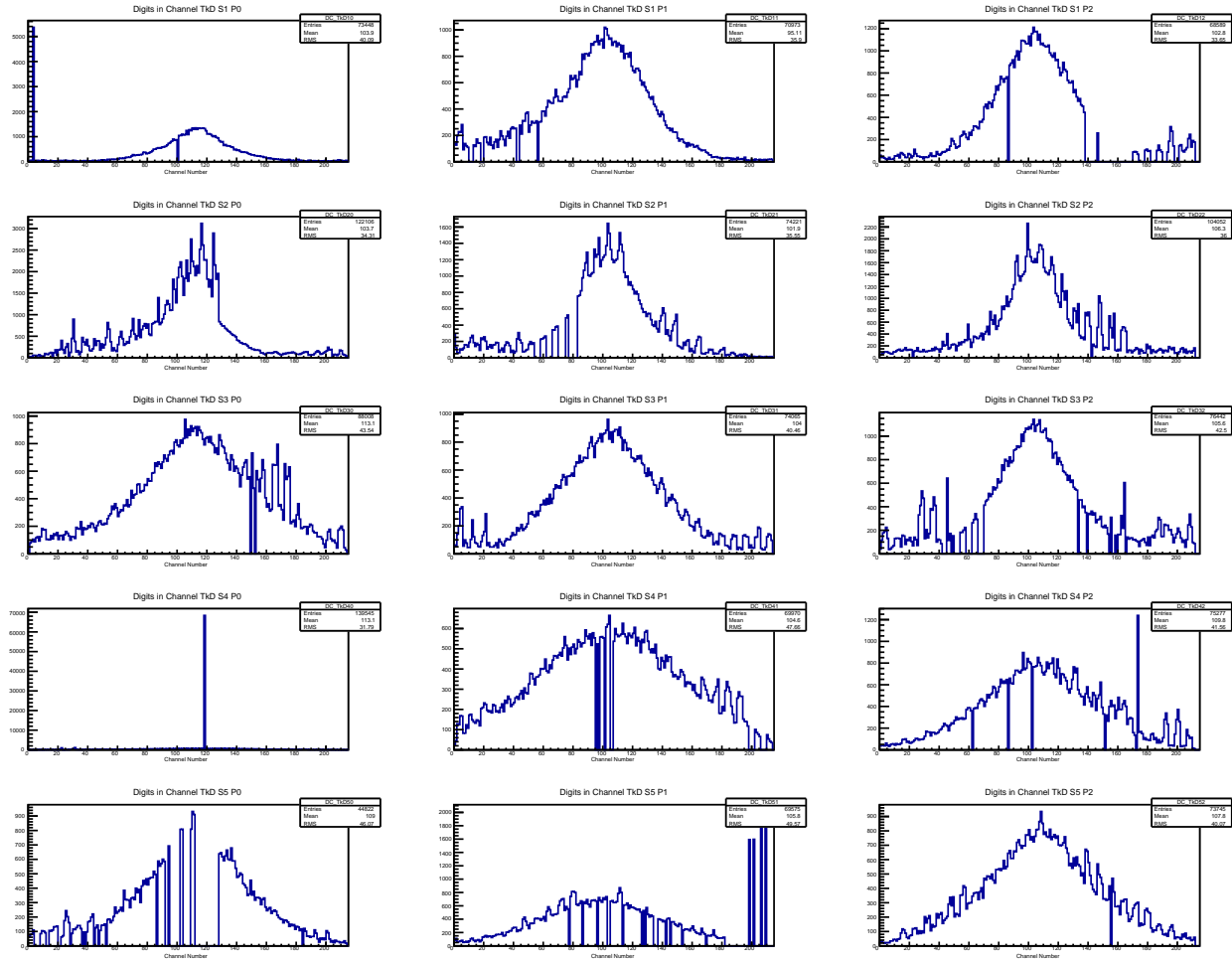


Figure 21:

## 230 6.2.2 Noise

Noise at electronics level discussion, 1/2 page, Chris H and Noise from data, 1/2 page, Chris H

## 6.2.3 Track Finding Efficiency

Track selection/Kalman, efficiency (from all data runs plotted by pt and if all equal just 10mm can be shown)  
resolution (from MC), reference MAUS and Tracker SW paper, 1 page, Chris H.

## 235 6.2.4 Track Fit Predicted Performance

Monte Carlo simulation used with realistic field and beam conditions in order to estimate the reconstruction performance. Run number 09964 was used, representing a typical data set used for the study of emittance evolution.

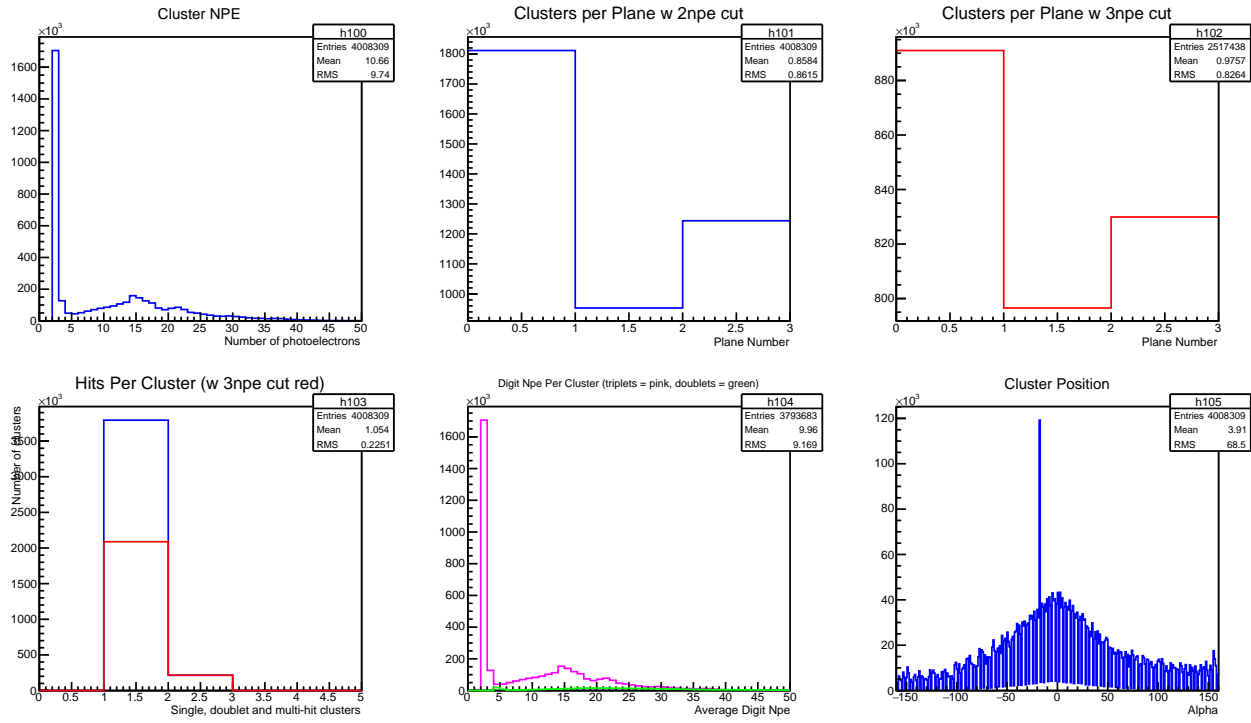


Figure 22:

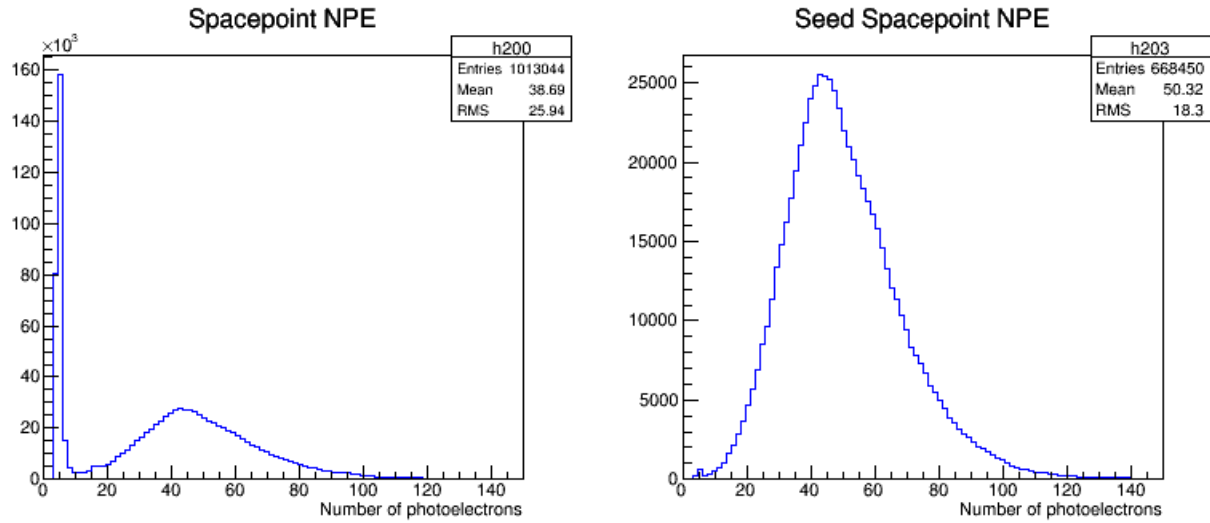


Figure 23: [left] The NPE of each spacepoint in the US and DS trackers combined. [Right] only the NPE of those spacepoints which go on to make tracks in the US and DS trackers combined are shown.

### 6.3 Tracker Efficiency Evolution

240 Tracker efficiency with time (maybe 1 runs every 3 months since start shown?), 1/2 page, Paul K.

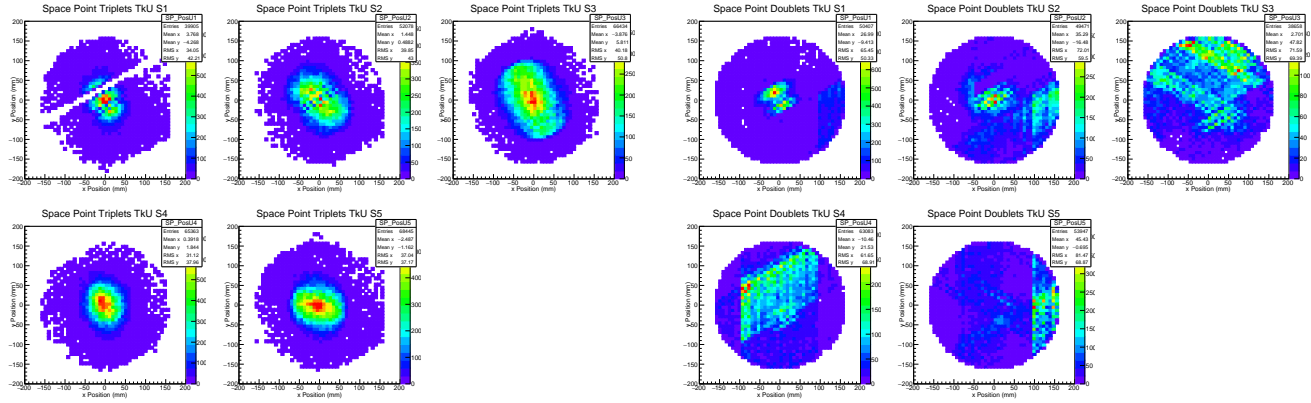


Figure 24:

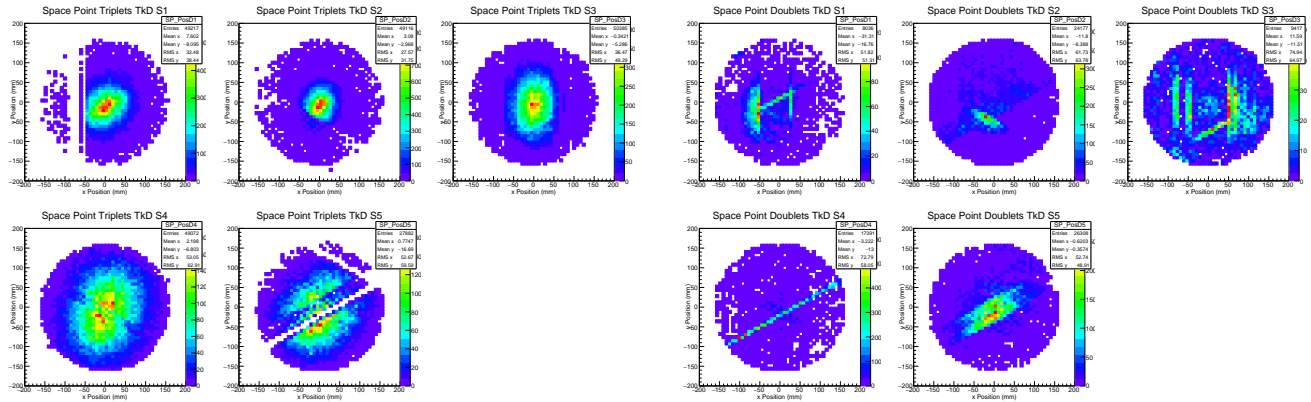


Figure 25:

## 7 PID

### 7.1 Introduction

### 7.2 Performance of the PID

## 8 Track Matching

### 8.1 Global reconstruction

The overall detector performance can be validated by extrapolating tracks from one detector to another and comparing the reconstructed coordinates with the extrapolated values. Tracks measured in the upstream tracker are extrapolated upstream to ToF1 and ToF0, and downstream to TKD and ToF2. Where there are materials in the beamline, the energy change on passing through the material is estimated using the most probable energy loss. Material thicknesses are approximated by the on-axis thickness.

Asymmetric effects can be introduced due to scattering from the walls of the cooling channel as the beam is not symmetric in the channel. In order to minimise the effects of such scattering, only events whose projected trajectory is significantly distant from the apertures are considered in this analysis. The following sample selection is considered:

- Downstream sample: Events must be included in the downstream sample to be considered in this analysis

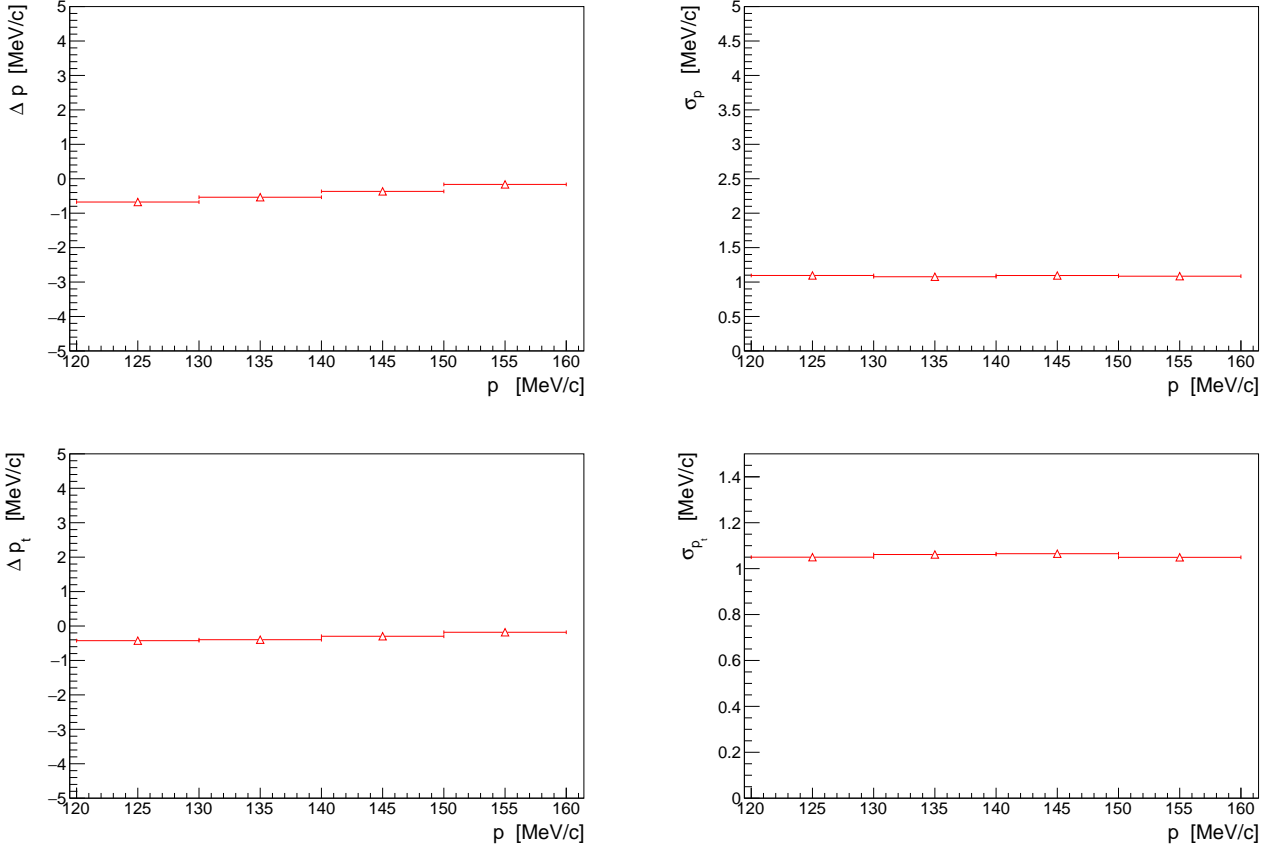


Figure 26: Predicted momentum reconstruction bias (left) and resolution (right) for the longitudinal (top) and transverse (bottom) momentum components in the upstream tracker.

- Aperture cut: The projected upstream track must be within 100 mm radius from the beam axis at the following apertures: the upstream absorber safety window; the upstream absorber window; the absorber centre; the downstream absorber window; the downstream absorber safety window; the upstream edge of SSD; the Helium window in SSD; the downstream edge of the downstream PRY aperture. This is performed even when the LH2 absorber was not installed, for the sake of consistency and because in some instances mounting flanges can limit the aperture and consistency.
- 1 space point in ToF2: The event must have exactly one space point in ToF2.
- Successful track extrapolation to ToF2: The projected upstream track must have been successfully extrapolated to ToF2

The sample sizes are shown for data in table 2 and 3. The equivalent MC sample sizes are listed in 4 and 5.

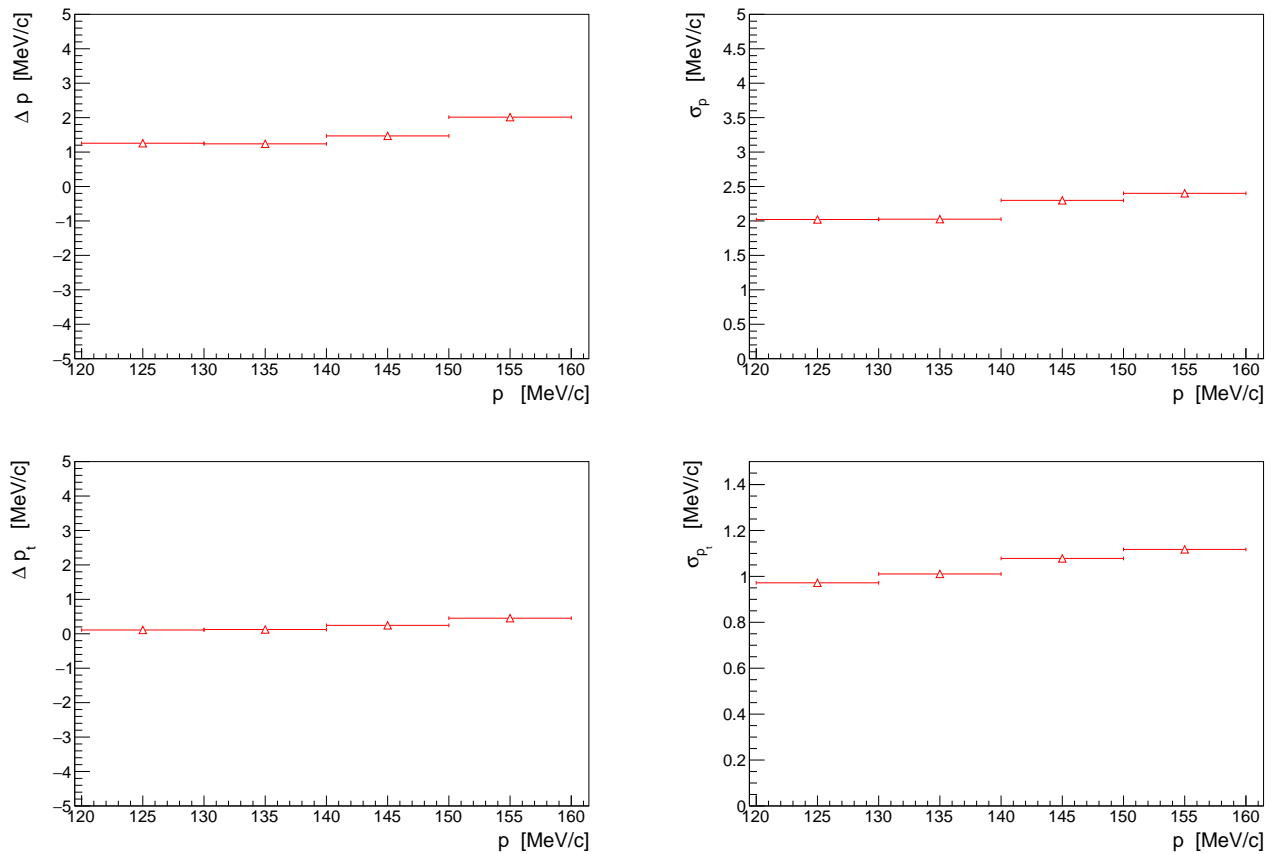


Figure 27: Predicted momentum reconstruction bias (left) and resolution (right) for the longitudinal (top) and transverse (bottom) momentum components in the downstream tracker.

Table 2: The extrapolated reconstructed data sample is listed. Samples are listed for 3-140 and 4-140 datasets.

|                                  | 2017-2.7<br>3-140<br>None | 2017-2.7<br>3-140<br>IH2<br>empty | 2017-2.7<br>3-140<br>IH2<br>full | 2017-2.7<br>3-140<br>LiH | 2017-2.7<br>4-140<br>None | 2017-2.7<br>4-140<br>IH2<br>empty | 2017-2.7<br>4-140<br>IH2<br>full | 2017-2.7<br>4-140<br>LiH |
|----------------------------------|---------------------------|-----------------------------------|----------------------------------|--------------------------|---------------------------|-----------------------------------|----------------------------------|--------------------------|
| Downstream Sample                | 13019                     | 8688                              | 9058                             | 11918                    | 29712                     | 23726                             | 8407                             | 24024                    |
| Cooling channel aperture cut     | 7203                      | 4721                              | 5166                             | 6836                     | 17731                     | 14571                             | 4935                             | 14293                    |
| One space point in ToF2          | 6935                      | 4506                              | 4885                             | 6477                     | 16800                     | 13817                             | 4596                             | 13362                    |
| Successful extrapolation to TKD  | 6935                      | 4506                              | 4885                             | 6477                     | 16800                     | 13817                             | 4596                             | 13362                    |
| Successful extrapolation to ToF2 | 6935                      | 4506                              | 4885                             | 6477                     | 16800                     | 13817                             | 4596                             | 13362                    |
| Extrapolation Sample             | 6935                      | 4506                              | 4885                             | 6477                     | 16800                     | 13817                             | 4596                             | 13362                    |

Table 3: The extrapolated reconstructed data sample is listed. Samples are listed for 6-140 and 10-140 datasets.

|                                  | 2017-2.7<br>6-140<br>None | 2017-2.7<br>6-140<br>IH2<br>empty | 2017-2.7<br>6-140<br>IH2<br>full | 2017-2.7<br>6-140<br>LiH | 2017-2.7<br>10-140<br>None | 2017-2.7<br>10-140<br>IH2<br>empty | 2017-2.7<br>10-140<br>IH2<br>full | 2017-2.7<br>10-140<br>LiH |
|----------------------------------|---------------------------|-----------------------------------|----------------------------------|--------------------------|----------------------------|------------------------------------|-----------------------------------|---------------------------|
| Downstream Sample                | 27025                     | 17783                             | 29577                            | 31257                    | 14847                      | 7278                               | 14784                             | 17138                     |
| Cooling channel aperture cut     | 15238                     | 10129                             | 16045                            | 17122                    | 5633                       | 2837                               | 5057                              | 6075                      |
| One space point in ToF2          | 14432                     | 9479                              | 14826                            | 15774                    | 5276                       | 2614                               | 4471                              | 5372                      |
| Successful extrapolation to TKD  | 14432                     | 9479                              | 14826                            | 15774                    | 5276                       | 2614                               | 4471                              | 5372                      |
| Successful extrapolation to ToF2 | 14432                     | 9479                              | 14826                            | 15774                    | 5276                       | 2614                               | 4471                              | 5372                      |
| Extrapolation Sample             | 14432                     | 9479                              | 14826                            | 15774                    | 5276                       | 2614                               | 4471                              | 5372                      |

Table 4: The extrapolated reconstructed simulated sample is listed. Samples are listed for 3-140 and 4-140 datasets.

|                                  | Simulated<br>2017-2.7<br>3-140<br>None | Simulated<br>2017-2.7<br>3-140<br>IH2<br>empty | Simulated<br>2017-2.7<br>3-140<br>IH2<br>full | Simulated<br>2017-2.7<br>3-140<br>LiH | Simulated<br>2017-2.7<br>4-140<br>None | Simulated<br>2017-2.7<br>4-140<br>IH2<br>empty | Simulated<br>2017-2.7<br>4-140<br>IH2<br>full | Simulated<br>2017-2.7<br>4-140<br>LiH |
|----------------------------------|--|--|---|---------------------------------------|--|--|---|---------------------------------------|
| Downstream Sample                | 8585                                   | 8567   | 8511  | 8624                                  | 18247                                  | 18247  | 18455   | 18553                                 |
| Cooling channel aperture cut     | 5112                                   | 4715   | 5032  | 5378                                  | 10884                                  | 10997  | 10758   | 10404                                 |
| One space point in ToF2          | 4540                                   | 4184   | 4499  | 4820                                  | 9544                                   | 9747   | 9467  | 9117                                  |
| Successful extrapolation to TKD  | 4540                                   | 4184   | 4499  | 4820                                  | 9544                                   | 9747   | 9467  | 9117                                  |
| Successful extrapolation to ToF2 | 4540                                   | 4184   | 4499  | 4820                                  | 9544                                   | 9747   | 9467  | 9117                                  |
| Extrapolation Sample             | 4540                                   | 4184   | 4499  | 4820                                  | 9544                                   | 9747   | 9467  | 9117                                  |

Table 5: The extrapolated reconstructed simulated sample is listed. Samples are listed for 6-140 and 10-140 datasets.

|                                  | Simulated<br>2017-2.7<br>6-140<br>None | Simulated<br>2017-2.7<br>6-140<br>IH2<br>empty | Simulated<br>2017-2.7<br>6-140<br>IH2<br>full | Simulated<br>2017-2.7<br>6-140<br>LiH | Simulated<br>2017-2.7<br>10-140<br>None | Simulated<br>2017-2.7<br>10-140<br>IH2<br>empty | Simulated<br>2017-2.7<br>10-140<br>IH2<br>full | Simulated<br>2017-2.7<br>10-140<br>LiH |
|----------------------------------|--|--|---|---------------------------------------|---|---|--|--|
| Downstream Sample                | 17810                                  | 18031  | 18188   | 18259                                 | 8843                                    | 9029  | 9155   | 9294                                   |
| Cooling channel aperture cut     | 10289                                  | 10071  | 9449  | 9906                                  | 3424                                    | 3393  | 3227   | 3337                                   |
| One space point in ToF2          | 9014                                   | 8766   | 8219  | 8577                                  | 2941                                    | 2926  | 2772   | 2861                                   |
| Successful extrapolation to TKD  | 9014                                   | 8766   | 8219  | 8577                                  | 2941                                    | 2926  | 2772   | 2861                                   |
| Successful extrapolation to ToF2 | 9014                                   | 8766   | 8219  | 8577                                  | 2941                                    | 2926  | 2772   | 2861                                   |
| Extrapolation Sample             | 9014                                   | 8766   | 8219  | 8577                                  | 2941                                    | 2926  | 2772   | 2861                                   |

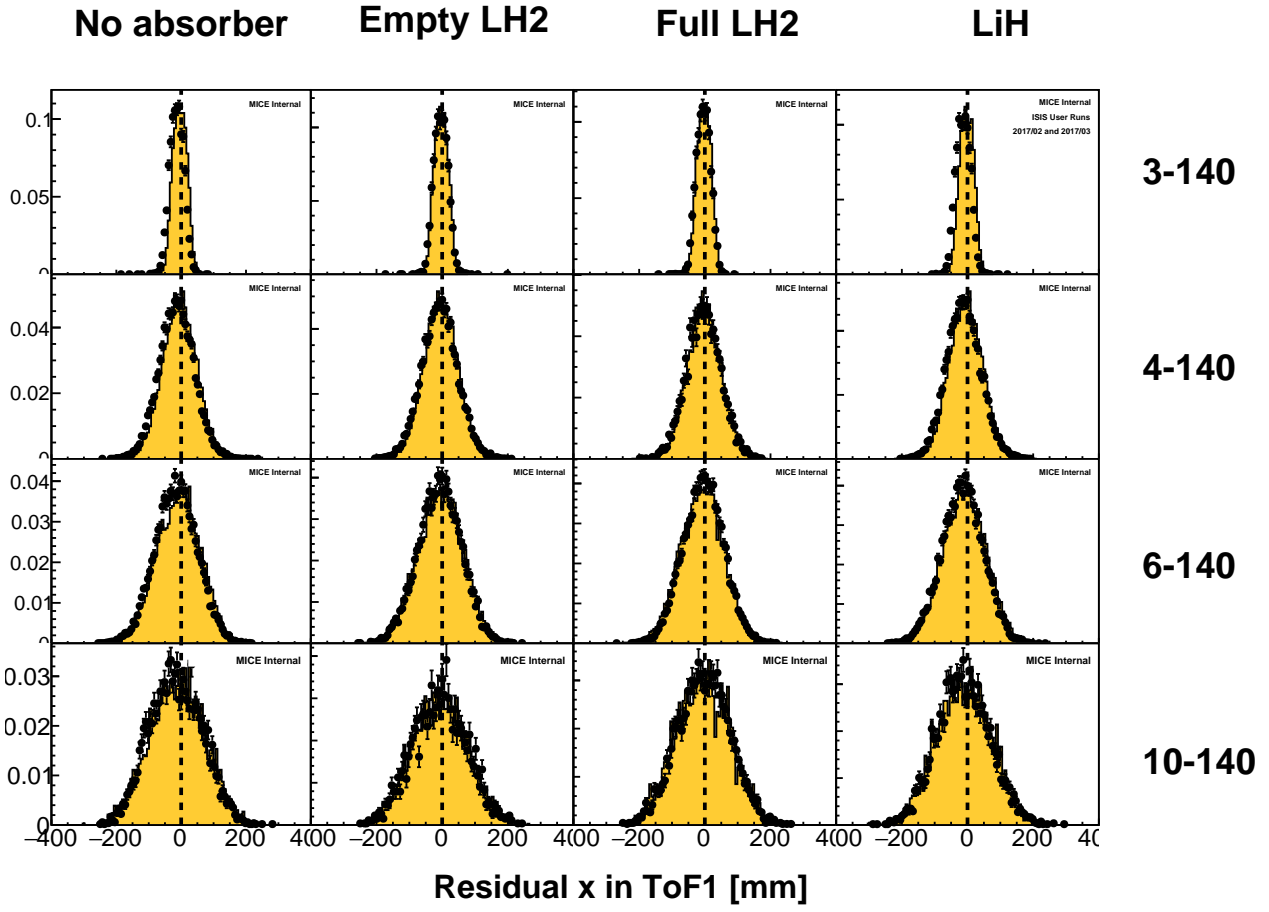


Figure 28: Residual horizontal (x) position in ToF1 of tracker tracks following extrapolation from TKU.

The extrapolated position following extrapolation to ToF1 is shown in fig. 28 and 29. In general the width of the distributions are comparable between MC and data. Where the diffuser is in place for higher emittance beams, the extrapolation goes through the diffuser material so the residuals are wider, owing to the increased scattering from the diffuser.

The time-of-flight residual in data shows a systematic offset from 0 and relative to the MC. The offset from 0 gets worse for higher emittance beams. It is thought to be an intrinsic property of the beam; muons that are scattered in materials between the tracker and the TOF have systematically shorter path lengths than the extrapolated trajectories, resulting in systematically longer extrapolated time of flight. The MC reconstruction is known to have issues, as evidenced by the discrepancy in slab  $dt$  for ToF0 and ToF1.

#### Plot momentum vs $dt$ for ToF01 and ToF12

Small misalignments between TKU extrapolated tracks and TKD are observed, indicated by the offset of transverse variables from 0, shown in fig. 31 and 32. There are known, uncorrected misalignments in the detector system and there are expected to be additional misalignments in the magnets which could lead to these offsets.

The total momentum shows discrepancy between TKU and TKD of about 1 MeV/c. This is consistent with the systematic offset in the tracker momentum resolution shown in fig. ?? and ???. It is interesting to note that the level of agreement between MC and data varies on a setting-by-setting basis in a statistically significant manner. Agreement is better for the settings where the liquid hydrogen windows were installed.

Further small misalignments are observed in the position residuals between TOF2 and tracks extrapolated

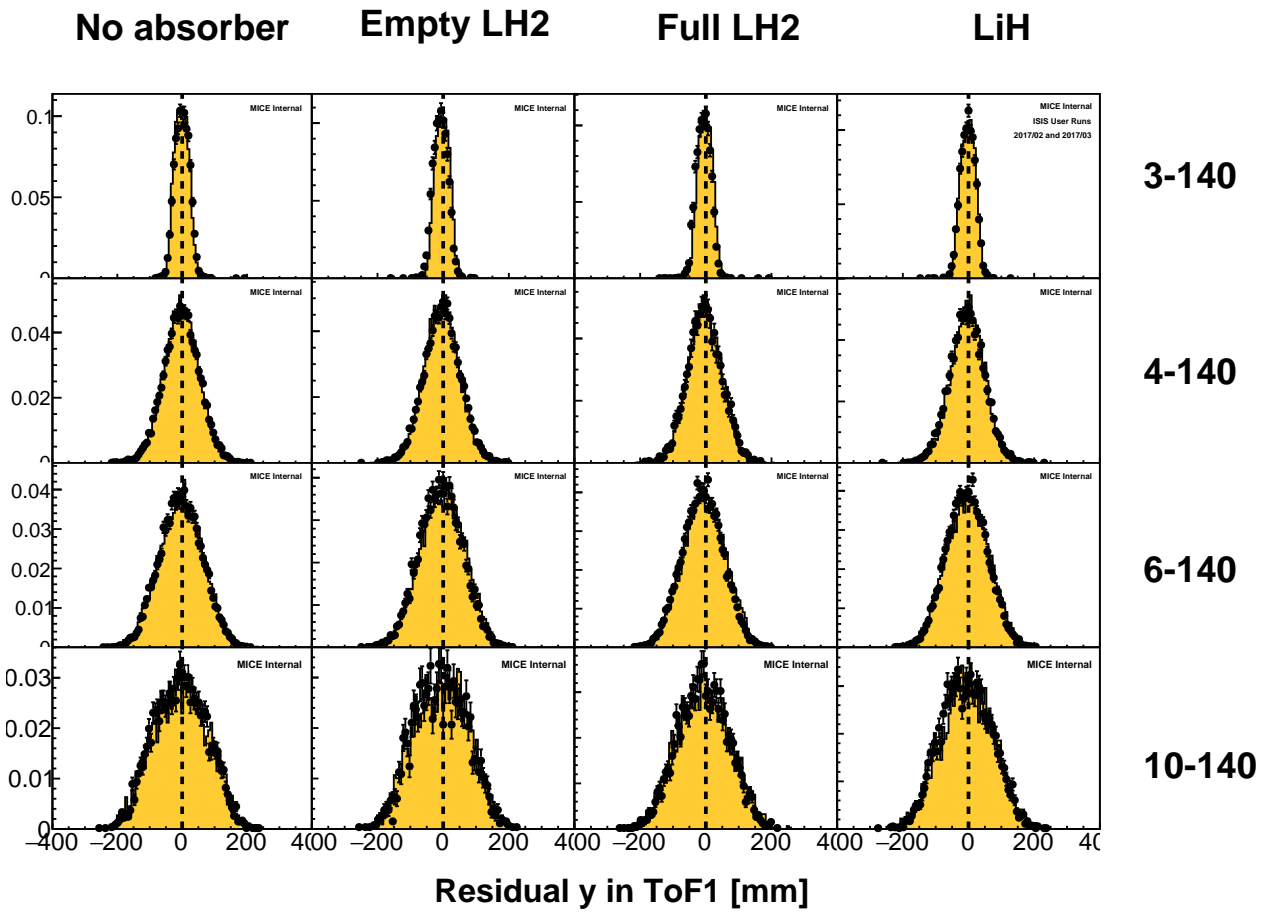


Figure 29: Residual vertical (y) position in ToF1 of tracker tracks following extrapolation from TKU.

285 from TKD. This is attributed to alignment issues.

TOF2 exhibits a significant offset from the extrapolated track.

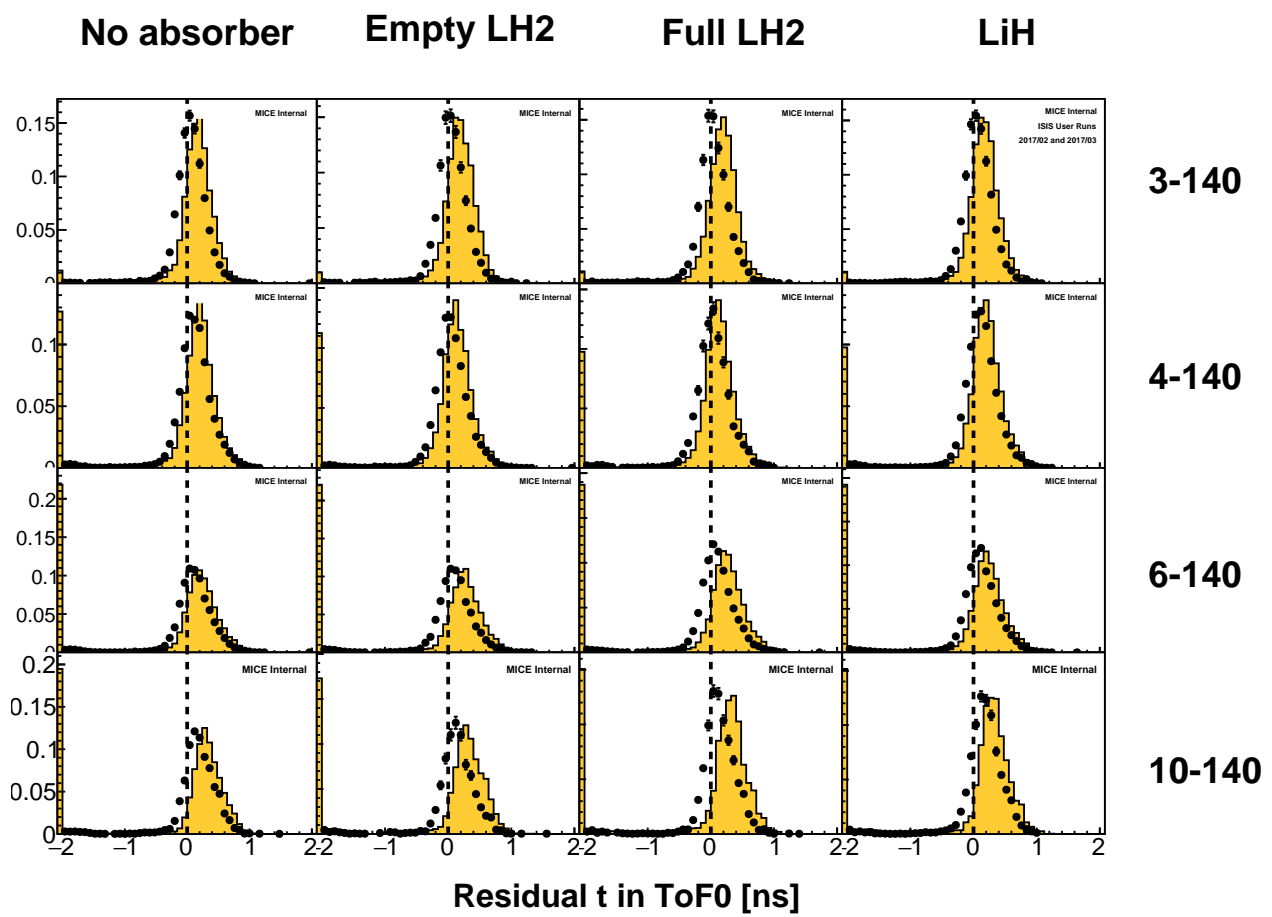


Figure 30: Residual ToF0 time of the extrapolated track. Track trajectories were drawn from TKU, while the track times were drawn from ToF1 with appropriate offsets for time-of-flight from TKU to ToF1 considered.

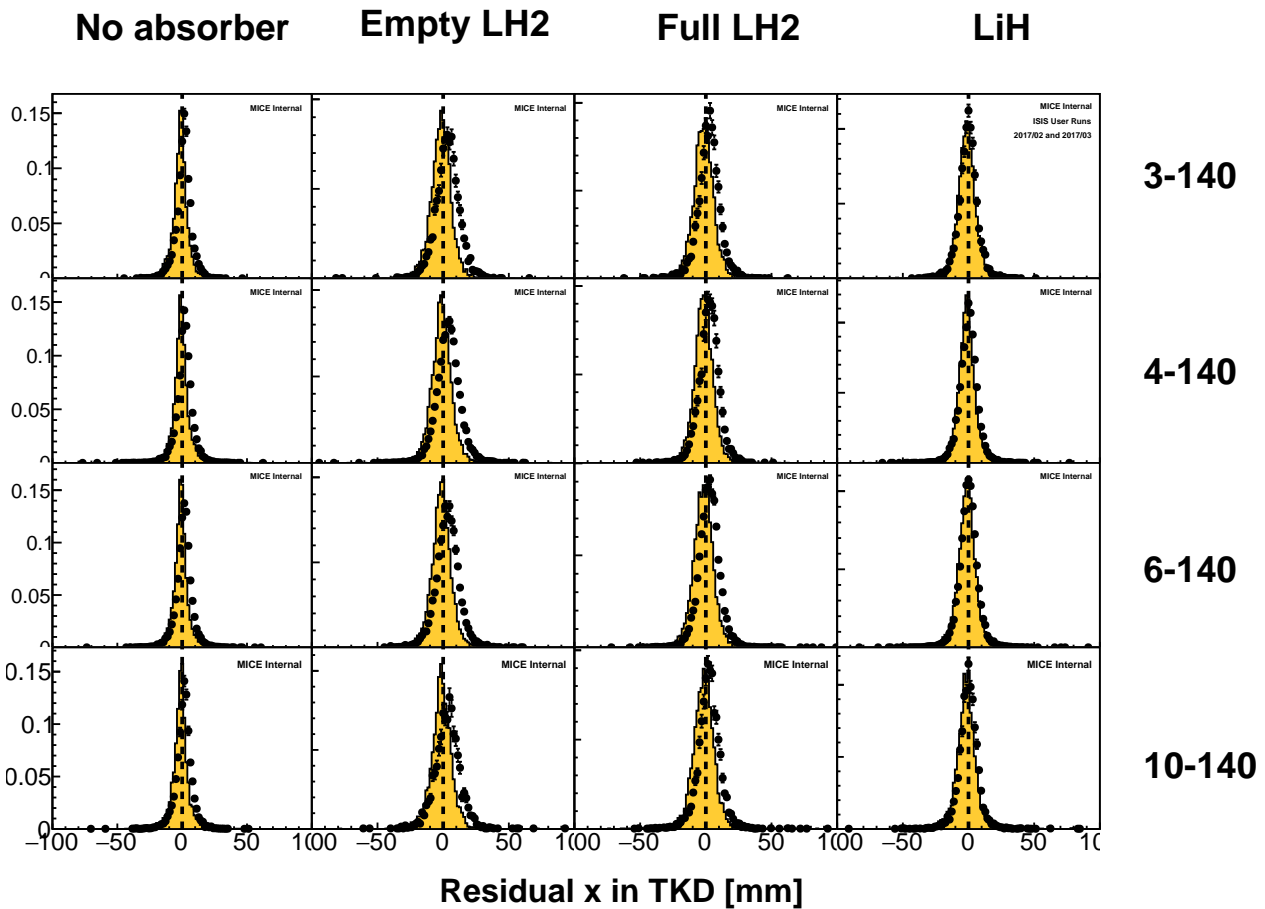


Figure 31: Residual  $x$  position of TKU tracks extrapolated to TKD, as compared to the tracks in TKD.

## 8.2 Beam based magnet alignment

## 9 Detector alignment

### 9.1 Introduction

## 290 9.2 Beam based detector alignment

## 10 Magnets and Beam Optics

### 10.1 Introduction

### 10.2 Beam based magnet alignment

### 10.3 Beam line optics

## 295 11 Absorber

### 11.1 Introduction

### 11.2 Validation of the absorber model

## 12 Conclusions

To be written at last.

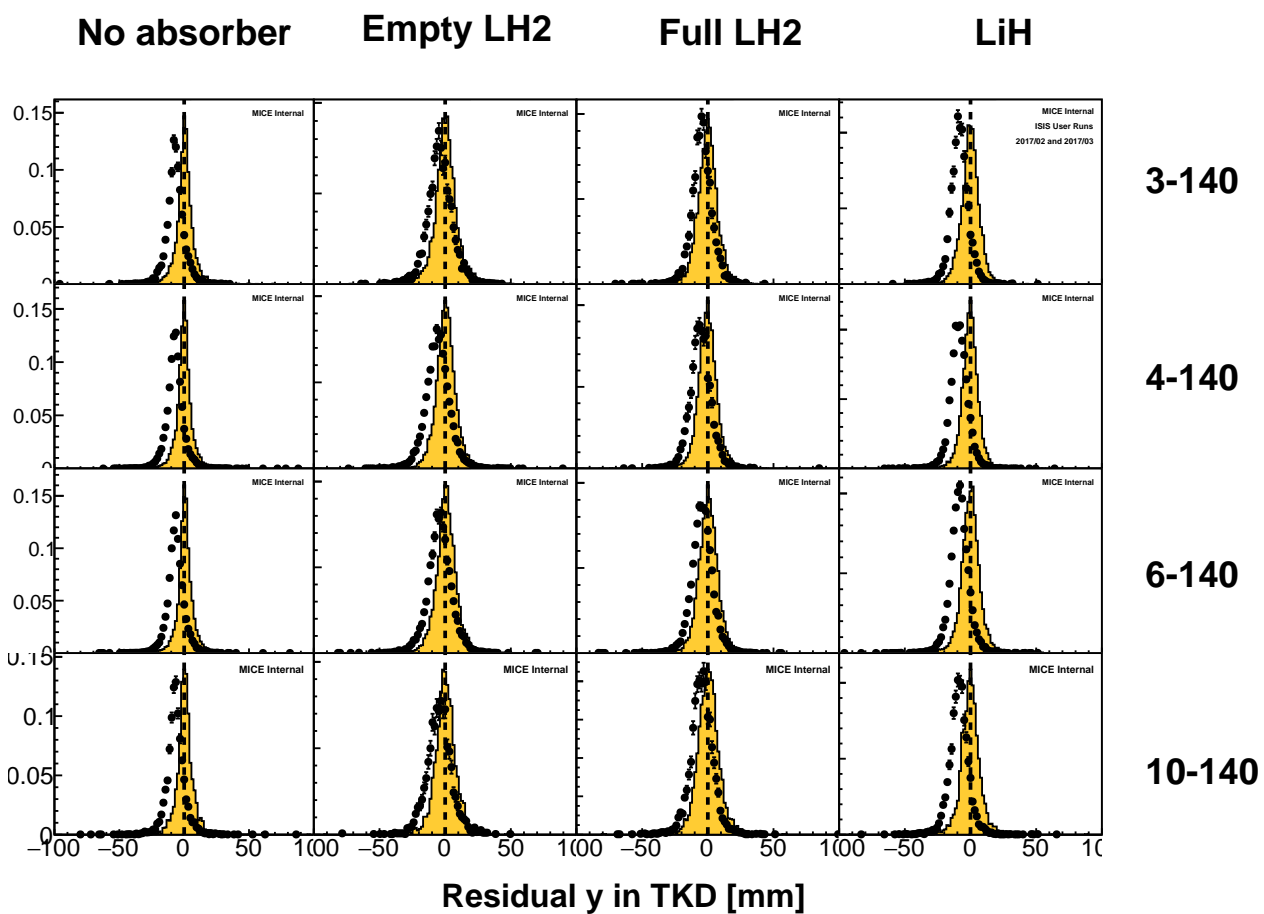


Figure 32: Residual  $y$  position of TKU tracks extrapolated to TKD, as compared to the tracks in TKD.

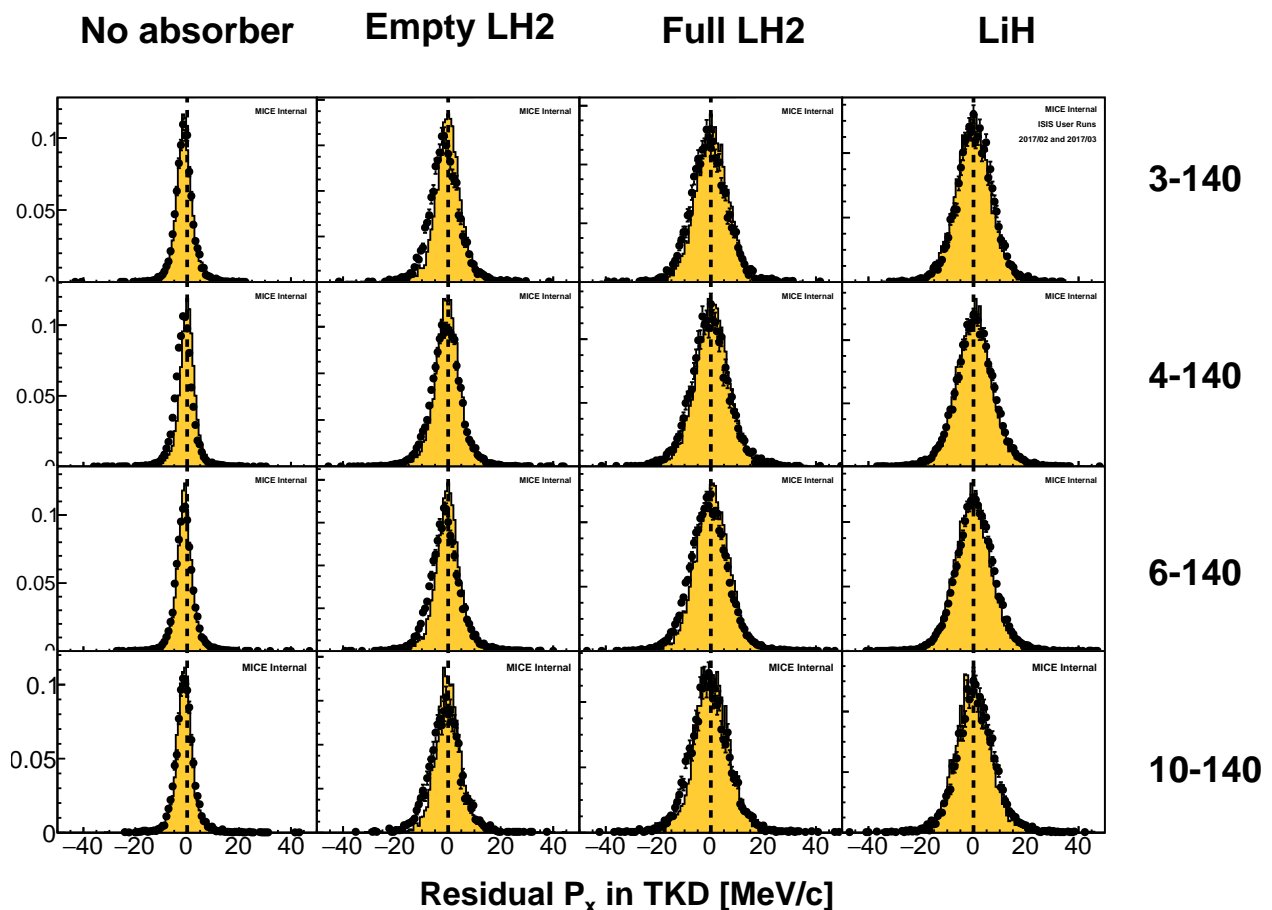


Figure 33: Residual  $p_x$  of TKU tracks extrapolated to TKD, as compared to the tracks in TKD.

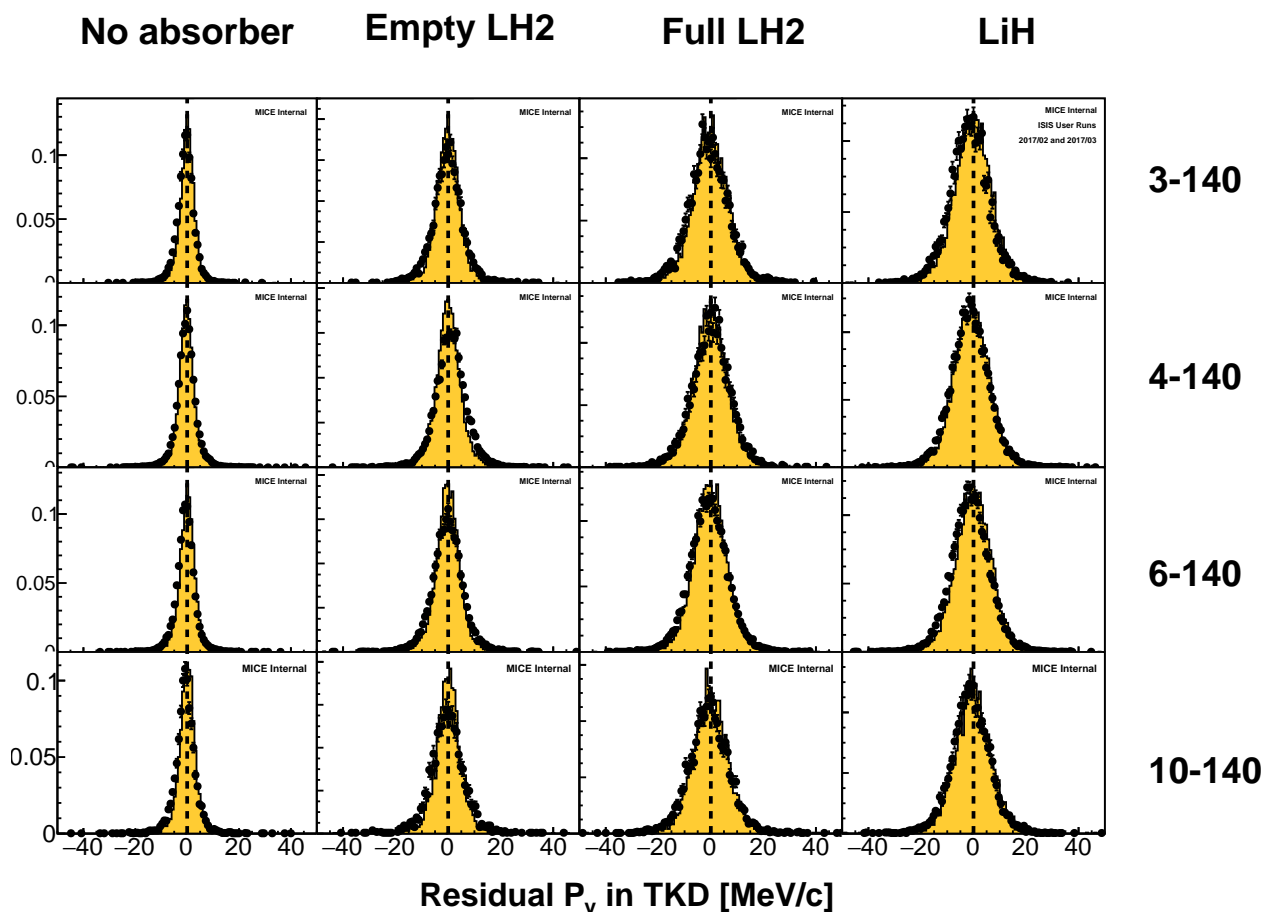


Figure 34: Residual  $p_y$  of TKU tracks extrapolated to TKD, as compared to the tracks in TKD.

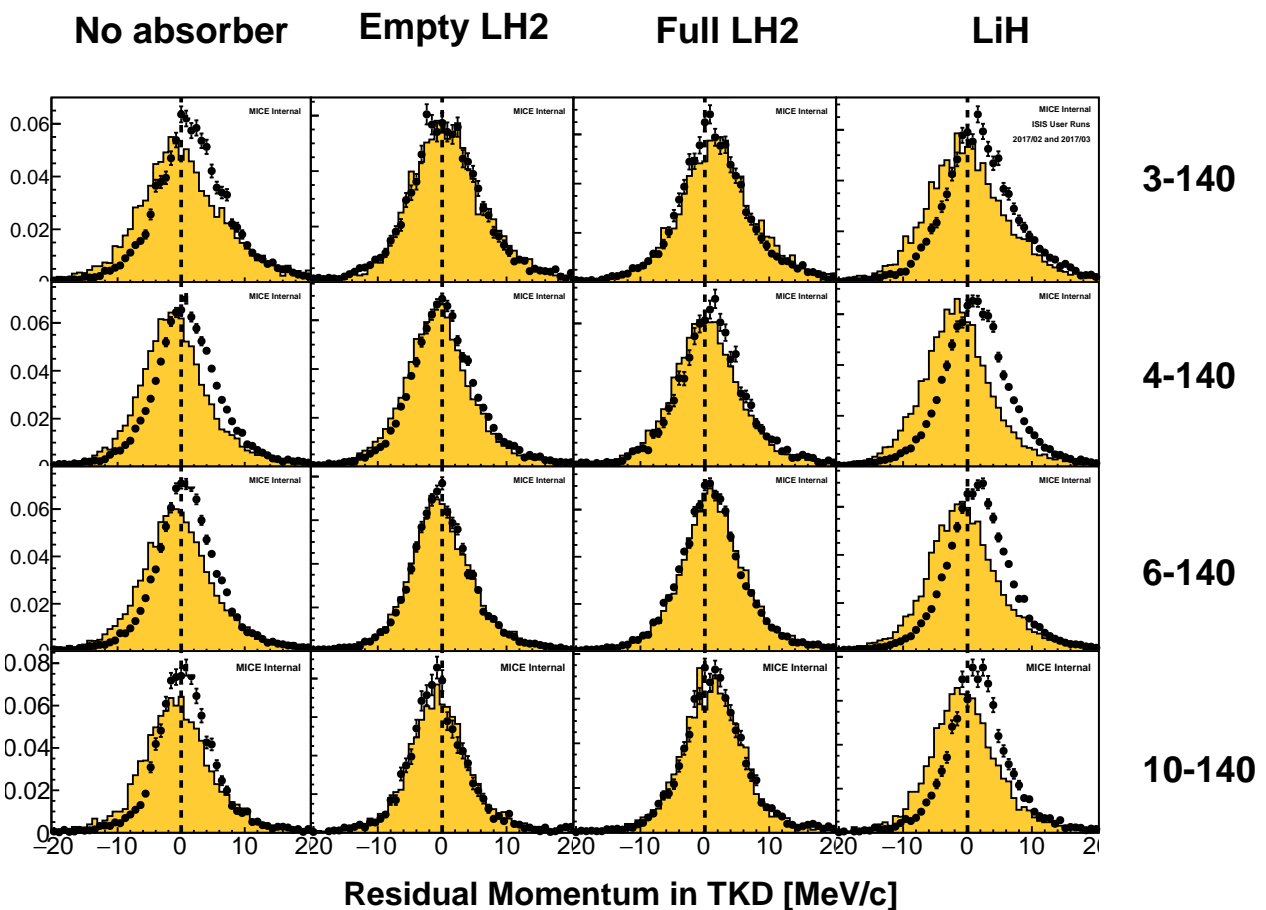


Figure 35: Residual  $p_{tot}$  of TKU tracks extrapolated to TKD, as compared to the tracks in TKD.

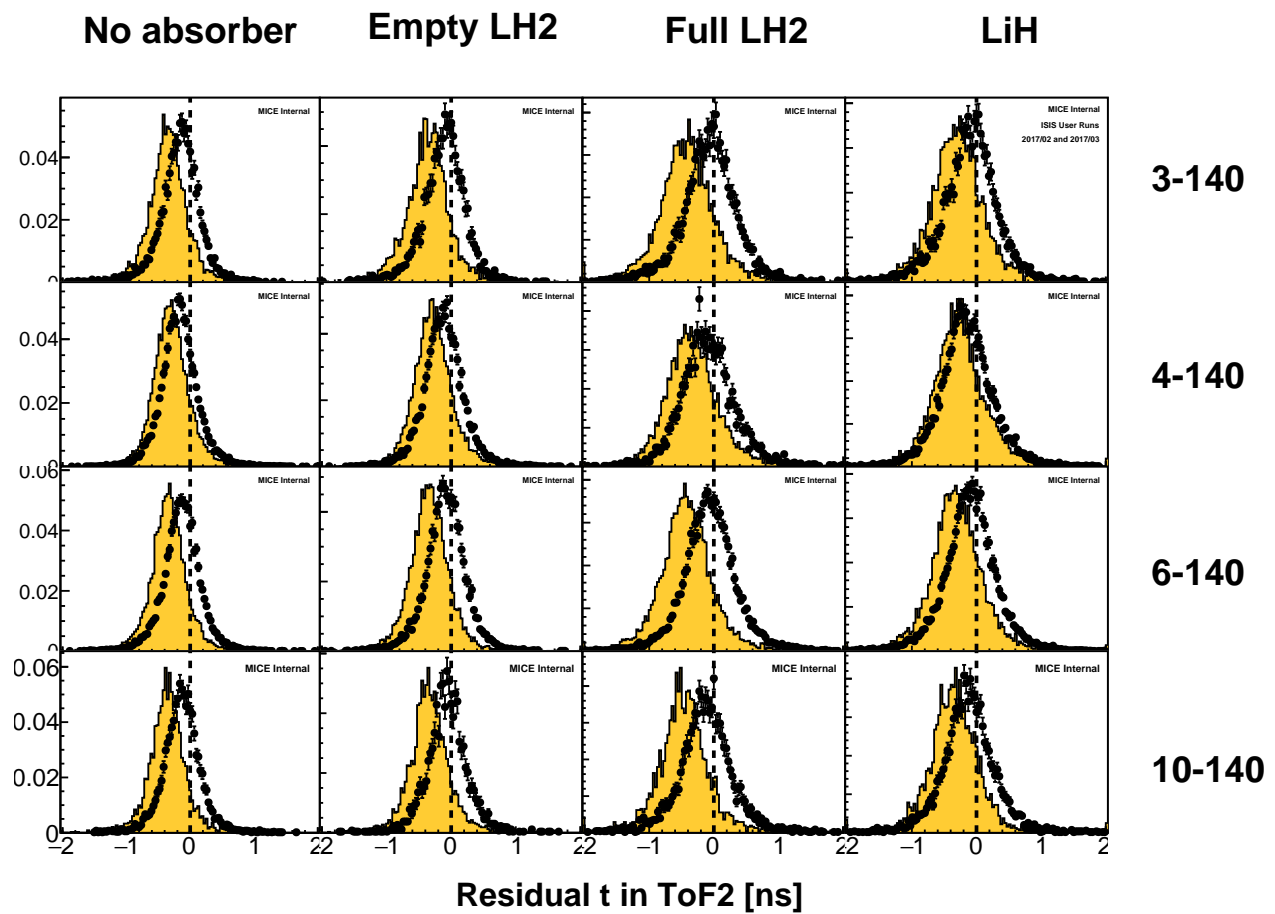


Figure 36: Residual time of TKU tracks extrapolated to ToF2, as compared to the time measured in ToF2. The track times were drawn from ToF1 with appropriate offsets for time-of-flight from TKU to ToF1 considered.

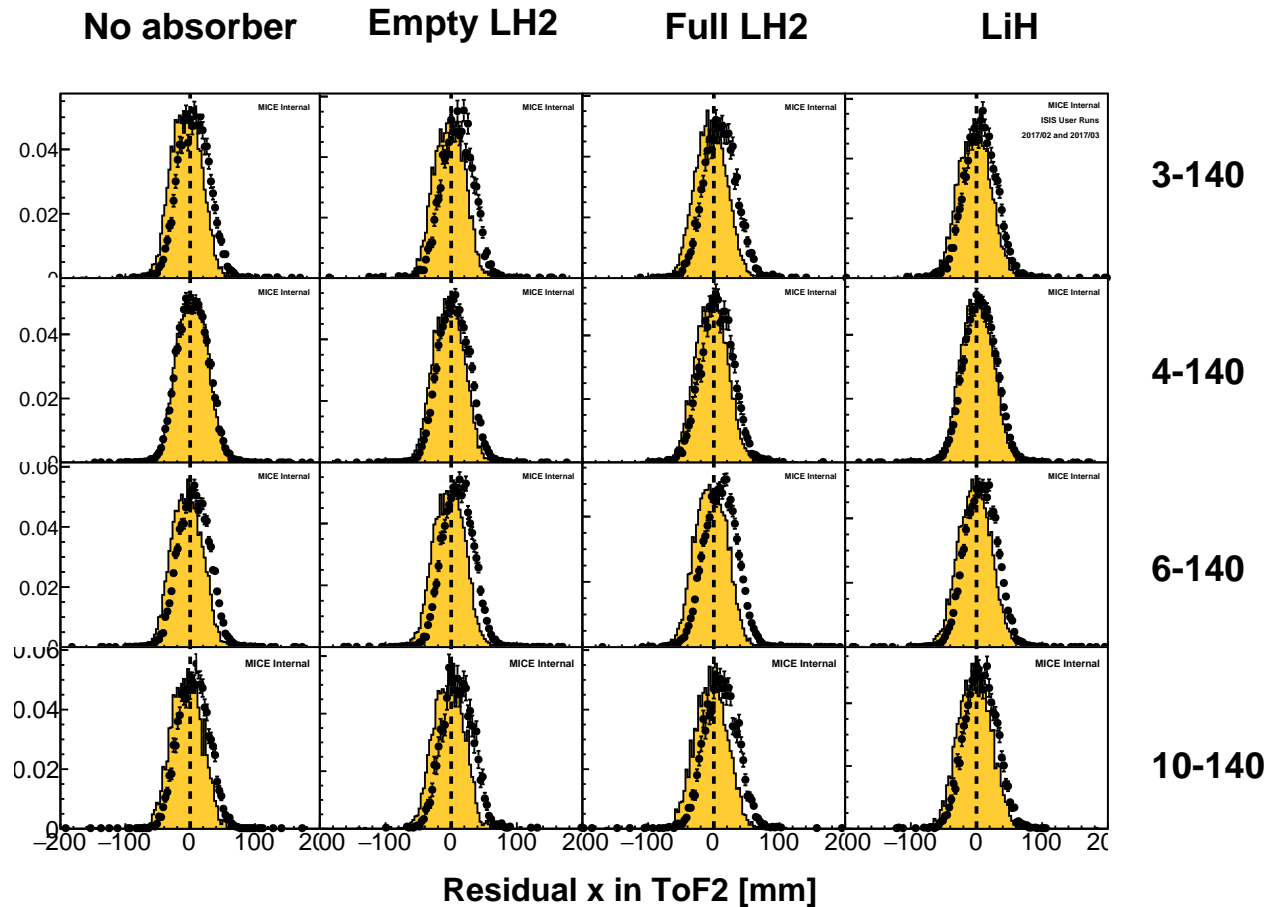


Figure 37: Residual  $x$  position of TKD tracks extrapolated to TOF2, as compared to the position measured in TOF2.

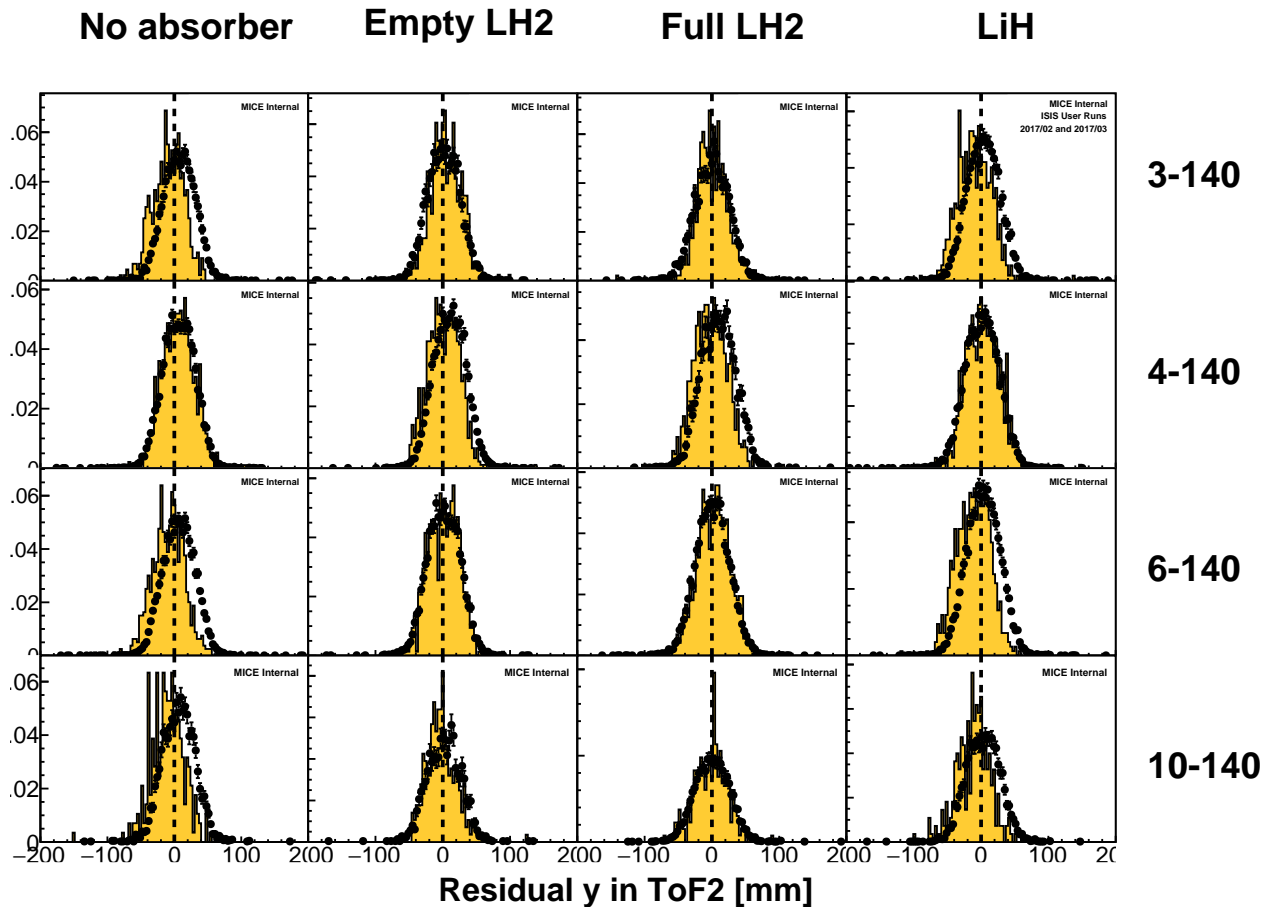


Figure 38: Residual  $y$  position of TKD tracks extrapolated to TOF2, as compared to the position measured in TOF2.

- [1] M. Bonesini, “The design of MICE TOF0 detector,” *MICE Note 145* (2006) .  
<http://mice.iit.edu/micenotes/public/pdf/MICE0145/MICE0145.pdf>.
- [2] R. Bertoni *et al.*, “The construction and laboratory tests for MICE TOF0/1 detectors,” *MICE Note 241* (2008) . <http://mice.iit.edu/micenotes/public/pdf/MICE0241/MICE0241.pdf>.
- 305 [3] R. Bertoni, A. Blondel, M. Bonesini, G. Cecchet, A. de Bari, J. S. Graulich, Y. Karadzhov, M. Rayner, I. Rusinov, R. Tsenev, S. Terzo, and V. Verguilov, “The design and commissioning of the MICE upstream time-of-flight system,” *Nuclear Instruments and Methods in Physics Research A* **615** (Mar., 2010) 14–26, arXiv:1001.4426 [physics.ins-det].
- [4] R. Bertoni *et al.*, “The construction of the MICE TOF2 detector,” *MICE Note 286* (2010) .  
<http://mice.iit.edu/micenotes/public/pdf/MICE0286/MICE0286.pdf>.
- 310 [5] D. Rajaram and V. C. Palladino, “The Status of MICE Step IV.”,  
<http://accelconf.web.cern.ch/AccelConf/IPAC2015/papers/thpf122.pdf>.
- [6] M. Bonesini, “Progress of the MICE experiment,” arXiv:1510.08825 [physics.acc-ph].
- [7] The MICE Collaboration, “Characterisation of the muon beams for the Muon Ionisation Cooling Experiment,” *ArXiv e-prints* (June, 2013) , arXiv:1306.1509 [physics.acc-ph].
- 315 [8] D. Adams *et al.*, “Pion contamination in the MICE muon beam,” *Journal of Instrumentation* **11** (Mar., 2016) P03001, arXiv:1511.00556 [physics.ins-det].
- [9] Y. Karadzhov *et al.*, “TOF detectors Time Calibration,” *MICE Note 251* (2009) .  
<http://mice.iit.edu/micenotes/public/pdf/MICE0251/MICE0251.pdf>.
- 320 [10] M. Bonesini, R. Bertoni, A. de Bari, and M. Rossella, “Behaviour in magnetic fields of fast conventional and fine-mesh photomultipliers,” *Nuclear Instruments and Methods in Physics Research A* **693** (Nov., 2012) 130–137, arXiv:1207.4909 [physics.ins-det].
- [11] M. Bonesini *et al.*, “The TOF1 local shielding,” *MICE Note 455* (2015) .  
<http://mice.iit.edu/micenotes/public/pdf/MICE0455/MICE0455.pdf>.
- 325 [12] L. Cremaldi *et al.*, “Progress on Cherenkov Reconstruction in MICE,” *MICE Note 473* (2015) .  
<http://mice.iit.edu/micenotes/public/pdf/MICE0473/MICE0473.pdf>.
- [13] R. Asfandiyarov *et al.*, “The design and construction of the MICE Electron-Muon Ranger,” *Journal of Instrumentation* **11** (Oct., 2016) T10007, arXiv:1607.04955 [physics.ins-det].
- [14] F. Drielsma, “Electron-Muon Ranger: hardware characterization,” Master’s thesis, University of Geneva, 330 2014. <https://arxiv.org/abs/1710.06946>.
- [15] D. Adams *et al.*, “Electron-muon ranger: performance in the MICE muon beam,” *Journal of Instrumentation* **10** (Dec., 2015) P12012, arXiv:1510.08306 [physics.ins-det].